Fourier-transform rheology and printability maps of complex fluids for three-dimensional printing

[1,2]*Esther García-Tuñón**, [1,2]*Rishav Agrawal*, [1,2]*Bin Ling* and [3]*David J C Dennis*

[1]*School of Engineering*, [2]*Materials Innovation Factory, University of Liverpool, The Quadrangle, L69 3GH, Liverpool, UK*

[3]*Interdisciplinary Center for Fluid Dynamics (NIDF/UFRJ), Rúa Moniz Aragão, 360, 21941-594, Rio de Janeiro, Brasil*

Corresponding author: *egarciat@liverpool.ac.uk

ABSTRACT

Direct ink writing (DIW) is a three-dimensional (3D) printing technique exploited by researchers working in fields from scaffolds for energy applications to bioprinting. DIW's main strength is that it enables shaping advanced materials, if these materials can be formulated into complex fluids that meet the demands of the printing process. They must be extremely shear thinning soft solids, able to flow through narrow nozzles, recovering their structure upon deposition and retaining the predesigned 3D shape. Formulation design and rheology are critical, but these aspects can be overlooked due to the high specialisation required. This work provides insights on the rheology and printability of complex yield stress fluids through the study of linear and nonlinear behaviours using large amplitude oscillatory shear (LAOS) rheology. We refine previous protocols and develop tools to understand the behaviours of formulations for DIW. We apply an existing mathematical framework to a library of carbon-based formulations for energy applications. Fourier transform (FT) analysis enables quantifying the onset and rising of higher harmonic contributions. Quantitative comparisons between different formulations are established using 3D harmonics maps, stress-strain plots, and material measures of nonlinearities (Fourier and Chebyshev coefficients, elastic moduli (G'_M, G'_L) and dimensionless index of nonlinearity (S)). 3D Lissajous plots provide a qualitative alternative to interpretate the yielding transition. We create Ashby-type printability maps to guide formulation design and elucidate that non-printable formulations show distinctive features. These insights on yield stress fluids for DIW are relevant to other applications and technologies: drilling fluids, gels, colloids, and foods.

Keywords: LAOS (large amplitude oscillatory shear), nonlinearities, FT-rheology, Lissajous, carbon materials, printability.

I. INTRODUCTION

Direct ink writing (DIW), a three-dimensional (3D) printing technique that relies on the formulation and design of complex (yield stress) fluids, is an expanding multi-disciplinary research field with a growing number of applications, from two-dimensional (2D) materials such as graphene-based materials and transition metal carbides and nitrides (MXenes) for energy devices,[1-4] and composites[5, 6] to self-healing polymers and gels for tissue engineering.[7-10] The potential of these applications is huge, and this is evidenced by the large multi-disciplinary community embracing this technology. One of DIW's main pitfalls is the limited understanding of the complex fluids that must be carefully designed for successful printing. To advance the field and fully exploit these applications it is crucial to achieve fundamental understanding of the complex fluids that underpin these techniques. DIW requires soft solids, yield stress fluids that can flow on demand through narrow nozzles (extremely shear thinning) and that must recover their original structure and retain the designed shape upon deposition in very short timescales. Despite the progress made in the

field and the increasing number of researchers working in this area, there are still very few published studies that report an adequate and comprehensive rheological characterisation of the printable formulations. Often only a brief discussion of the formulation's "viscosity" or a flow curve is provided, while some studies do not include any characterisation at all. Those studies in which the rheology is reported, quite often lack a clear and relevant analysis, and the quality of the data reported could be questioned. The specialisation required for the formulation and characterisation of printable materials limits the roll-out of this technology, compared to readily available off-the-shell additive manufacturing techniques such as inject printing, fused deposition modelling or stereolithography. There is a need to improve the quality of the data[11] reported and their analysis to deepen our fundamental understanding of such complex fluids. The quest on understanding yield stress fluids is common to many other applied research areas, for example drilling fluids,[12] foods,[13] biological fluids,[14, 15] and soft matter[16, 17] in general, which supports and strengthens the motivation and purpose of this work.

Complex fluids for DIW are formulated through many different approaches including Poloxamer® gels (Pluronic® F127 is widely used),[10, 18] colloidal suspensions,[19] liquid crystals, 2D materials,[1, 20] and pH-responsive branched copolymer surfactants[3] to name a few. Among these, Poloxamers® F127 (referred to as F127 in this paper) is the additive most used because it is readily available, relatively inexpensive, and easy to formulate. It is also frequently used as a drug delivery system and in bioprinting.[7-10, 21] Graphene Oxide (GO) suspensions[22-26] are also used in DIW, but not as widely as F127 yet. GO and other 2D materials in suspension exhibit a unique and fascinating rheology, they display a wide range of behaviours from Newtonian to printable in a relatively small concentration range, between 0.01 and 3 vol%,[27] with the added benefits that they act as multi-functional additive to aid the printing of other materials,[22] and can also play a role as functional material upon thermal reduction to reduced GO (rGO).[4, 20, 28] The number of researchers using these materials (F127 and GO) as formulation base in DIW is rapidly growing and hence it is necessary to address current gaps in the field, deepening our fundamental understanding of these soft solids.

Previous studies[22, 27, 29, 30] and reviews[31] on this topic generally agree that complex fluids for DIW are yield-stress shear thinning fluids. The concept of 'printability' and the design of yield stress fluids is highly dependent on the context of each specific application. In bioprinting, for example, low stiffness (storage modulus, $G'(\gamma, \omega)$) and yield stress (σ_y) values are required to ensure cell viability.[9] While other applications will require a more accurate control of morphological features that can only be achieved through stiff formulations. However, the need for careful design and better understanding of yield stress fluids is common to all the applications that can be realised through DIW. Rheological studies have been done in continuous (flow ramps) and oscillatory shear, and the most reported rheological parameters are the storage modulus, $G'(\gamma, \omega)$ and yield stress, σ_y (note that sometimes it is referred to as the flow stress, σ_f). For these yield stress fluids, the σ_y values typically range between two orders of magnitude (~100 to 1000 Pa), and the $G'(\gamma, \omega)$ from ~1000Pa up to 1 GPa. We found that data collected in continuous shear for 'printable' formulations (or any other complex fluid with high yield stress values) are accompanied by large uncertainties[27] and other issues (such as shear fracture, shear banding and other transient effects) that make the data unsuitable for a reliable and quantitative analysis. We found that as we approach the 'printability' window, the flow behaviour index (*n,* dimensionless) values approach 0, and uncertainty increases dramatically.[27] An extended Cox-Merz rule can be used to correlate the frequency sweeps in oscillatory shear with continuous shear,[27] however the uncertainty of this rule also increases within the printability window. We also found that oscillatory tests on printable formulations are reliable and reproducible (with very small uncertainties),[22, 27] and they are also extremely versatile to probe our materials reducing the issues we find in continuous shear. LAOS has

been used within the DIW community, however the way it is reported is often incomplete, for example results might be provided without a description of how the test was done or a discussion of results. This makes very difficult to compare and rely on published data.

In previous work, we have performed structure evolution tests (combining time, frequency and amplitude sweeps); study their breakdown through large amplitude oscillatory shear (LAOS) tests; and their recovery through LAOS to SAOS transitions.[22, 27] We concluded that we can describe and predict the printability of a formulation based on the following parameters obtained from LAOS tests: the storage modulus within the Linear Viscosity Region (LVR), $G'_{@LVR}(\omega)$; the σ_f value at the solid-to-liquid transition (moduli crossover, $G'(\gamma,\omega) = G''(\gamma,\omega)$); and what we defined as the Flow Transition Index (FTI, dimensionless) that quantifies the yielding region.[27] These parameters can be used in Ashby-type charts to create printability maps. However, this simple approach might lead to flawed conclusions if the LAOS data are not carefully analysed. Although we believe that these 'maps' can and will be a useful tool (and indeed we include examples in the last section of this work), LAOS has much more to offer in DIW.[32, 33]

Here we study the rheology of a library of carbon-based formulations using Pluronic gels F127[10, 18] and GO suspensions[22, 27] as formulation base, which are then mixed with different active materials, including graphite (Gr, table I) and multi-walled carbon nanotubes (MWCNTs, referred to as CNTs for simplicity, table I). GO plays a dual role as a formulation base and active material. The formulations are designed with very specific concentrations (table II) that have been chosen from a previous systematic study.[34] The selection criteria was based on their final functional performance from electrical conductivity measurements, either as printed or after thermal-reduction. However, their functional performance is not the focus of this work, and its discussion will not be included. Here, we focus on rheological studies to compare the fingerprint of the formulation base (F127 or GO) and how the addition of different active materials (Gr and CNTs) changes these fingerprints. A detailed characterisation and discussion of the materials used is provided in the materials and methods section.

In this work, we use LAOS[32, 35] tests to characterise the yielding transition and nonlinear behaviours of the selected formulations designed for 3D printing of conductive architectures.[34] We use Fourier Transform (FT) analysis, and a mathematical framework to determine quantitative material measures of nonlinearities proposed by Ewoldt et al.[36] This approach enables us to quantify the onset of nonlinear behaviour (from the FT spectrum, in section III.B) and material measures of nonlinearities (section III.D, Fourier coefficients (G'_n, G''_n), Chebyshev coefficients (e_n, v_n), elastic moduli (G'_M, G'_L) and dimensionless index of nonlinearity (S), using higher FT-harmonics information. We compare our transient data analysis, with the correlation results provided by TRIOS, the software of the TA rheometer (section III.C). LAOS results are also used to analyse the yielding of printable and non-printable soft solids using a different perspective[37] that correlates LAOS and steady shear of soft solids at the onset of the fluid rheological behaviour. We complement these results with 3D (supporting information, *Lissajous Analysis* section) and 2D *Lissajous-Bowditch* (L-B) plots[38] (section III.F) that provide a visual approach to qualitatively interpretate quantitative material measures such as Fourier and Chebyshev coefficients. Section III.F focuses on printability maps, or Ashby[39] type charts based on data that can be obtained from a carefully analysed LAOS test, that can be used as a tool to guide formulation design. We aim to put our results in a wide context, but to the best of our knowledge, there are no other published studies focused on the formulations we study here; or any other quantitative LAOS FT-rheology studies on 3D printable formulations. We have found some examples of studies on high-yield stress fluids of the additives[40] and actives materials used in this work,[41] however they are not formulated at comparable concentrations. Due to the relatively small number of formulations

analysed, establishing a link between nonlinear parameters and 'printability' is beyond the breath of this study. The results presented here will demonstrate that LAOS and FT-rheology are powerful tools: 1) to understand the nonlinearity of complex fluids designed for DIW; 2) to quantify the boundaries of linear and nonlinear behaviours; and 3) to assess how the linear and nonlinear behaviour change when using different ingredients in the formulation. These analyses are a promising path to study the behaviour and performance of bespoke additives and to advance formulation development in the future.

II. MATERIALS AND METHODS

Materials. *Graphite powder (Gr). S*igma Aldrich 99% carbon basis with a particle diameter of <45 µm as stated on material data sheet (CAS no. 7782-42-5). The graphite raw powders have been sieved through 100 µm to aid the breakdown of aggregates and discard large particles before preparing the formulations. *Multi-walled carbon nanotubes powder (CNTs).* Sigma Aldrich, (multi-walled >90% carbon basis) with a diameter of 110-170nm, length of 5-9µm and density of 1.7g/mL as stated on the material data sheet (CAS no. 308068-56-6). *Graphene oxide (GO)***.** Graphene oxide solution (GO-4-2500) was purchased from *Graphenea* (Spain) and fully characterised. Some of the results are included in this manuscript; additional information can be found in previous work.[34] The pH of GO suspensions was determined using a S210 pH-meter (InLab Expert Pro-ISM), with values of ~ 2.2 for the GO stock solution. *Pluronic F127***.** Sigma-Aldrich, UK. CAS no. 9003-11-6.

Powder characterisation techniques. Dynamic light scattering (DLS) measurements were taken to measure the size distribution of the Gr powder (dispersed in distilled water) using a Malvern Mastersizer 3000. For GO, a small amount of sample was dispersed in distilled water and deposited between two glass slides for observation in an Olympus BX53 optical microscope. Lateral flake size was determined from individual (>200) flakes on several microscopy images using ImageJ, image analysis software. For CNTs, Scanning Electron Microscopy (SEM) images were taken in a Hitachi S4800 SEM, and used to determine their diameter with ImageJ. Gr and CNTs powders were uniaxially pressed using an Specac Uniaxial press with a max load of 2 ton, to make pellets with an average diameter of 8±1 mm. A concentrated GO suspension was deposited on a glass slide, evenly spread, and left to dry ensuring full coverage of the glass surface. Water contact angle (WCA) measurements were carried out using the sessile drop method in a Kruss DSA100 system. Gr and CNTs powders were degassed for 6 hours under vacuum prior nitrogen physisorption and Brunauer–Emmett–Teller (BET) surface area measurements in a Micromeritics 3 Flex. Elemental chemical analysis (Thermo Scientific Flash 2000 configured for %CHNS) on the GO commercial suspension provided the following composition: 45.9 wt% C, 1.9 wt% H and 0 wt% N with the rest being oxygen. This gives a C/O content of 0.88 which is higher than that of the GO used in previous works.[22, 27]

Materials characterisation results. Although the active materials (Gr, CNT) have similar densities (~1.7, 2.2 mg/ml) and composition (all carbon based), their shapes, sizes, wettability, and specific surface area are diverse playing a crucial role in the interparticle, and particle/solvent interactions and therefore in the formulation process, 3D printing behaviour, and functional performance. Each of the active materials used in this work has different intrinsic properties (such as particle size distribution, shape, specific surface, and wettability) that determine their behaviour and printability when mixed with our two formulation base systems: F127 and GO. GO has a dual role, as the additive to aid the printing of active materials, and as an active material itself after thermal reduction during post-processing. Here we include a summary (table I, figure 1) with the results of their characterisation using the techniques detailed in the previous subsection.

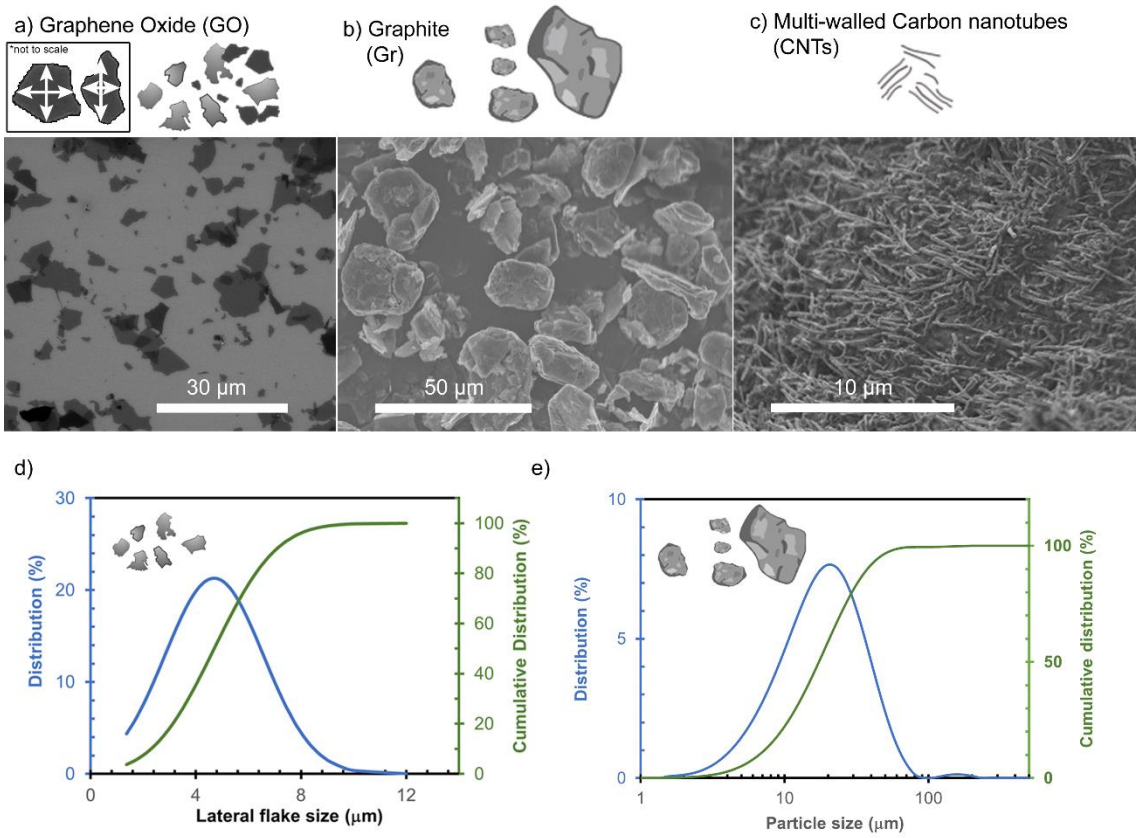

Figure 1. Raw materials characterisation results. Cartoons and scanning electron microscopy (SEM) images illustrating the morphological differences between the active materials: in (a) inset with a not to scale illustration of how the lateral flake size is determined (using two perpendicular lines (white arrows) across the centre of each flake) and SEM image for GO flakes (provided and owned by Graphenea SA); (b) graphite and (c) CNTs) of the active materials used to prepare the formulations in table II.[34] d) Lateral flake size distribution (%, normal and cumulative) determined from >200 counts measured in several optical images using ImageJ. e) Particle size distribution for Gr powders measured using DLS.

Table I. Summary of the characterisation of raw materials: Graphite (Gr), multi-walled carbon nanotubes (CNTs) and graphene oxide (GO). Lateral flake size of GO flakes, and CNTs diameter values have been measured through image analysis, Gr particle size distribution (average and standard deviation (from three different DLS measurements) for D_{50}, meaning 50% of the particles are below this size, also refer as median particle diameter, or median particle size) has been determined using DLS. WCA values for Gr and CNTs have been measured on the surface of uniaxially pressed pellets, and for GO on a thick film on a glass substrate.

Raw material	Particle size	BET (m^2/g)	WCA (°)
Gr	*D_{50}=18.3±0.2 µm	4.3±0.1	40±5
CNTs	D~105±22 nm	57.7±0.5	95±4
GO	Lateral flake size ~4.7±1.9 µm	--	52±1

In this work we use a commercial GO source unlike our previous published work.[22, 27] The commercial GO flakes have a considerable smaller lateral flake size (with lateral sizes ranging between ~1 and 12 µm for commercial GO, figure 1) compared to our previous work, in which we synthesised our own GO flakes (with lateral size ~64±40µm obtained from image analysis).[34] Lateral flake size has an impact in formulation performance and printability, larger flakes facilitate network formation but this can be compromised with smaller flakes.[42] Gr particles have an even wider particle size distribution (figure 1, table 1), with particles ranging

from ~1 to 100 µm (figure 1). A small number of larger particles and possibly aggregates are also present in the DLS analysis (figure 1). These larger particles are discarded in the sieving process.

Formulation of carbon materials for DIW.

Pluronic® F127 as a formulation base: Pluronic® F127 is a triblock copolymer of poly-propylene oxide (PPO) flanked by two poly-ethylene oxide blocks (PEO). Pluronic® solutions of block copolymers self-assemble to form micelles when reaching a critical micellar temperature (CMT). At sufficient concentrations, the triblock micelles associate above a critical gelation temperature (CGT) and form a lyotropic liquid crystalline (LLC) phase.[21] The PPO block dehydrates with temperature,[21] being hydrophobic at $T(℃) > T_{CGT}(℃)$ and hydrophilic at $T(℃) < T_{CGT}(℃)$ which is responsible for the thermo-reversible gelling behaviour. The gelation temperature depends on the type of Pluronic® and concentration.[21] F127 is a nearly Newtonian liquid at low temperature (below CMT and CGT) which makes it very easy to add and mix other components in the formulations. F127 becomes a printable hydrogel $T(℃) > T_{CGT}(℃)$~18℃ at a concentration of 25wt% in water.[4, 18, 43] Recent studies on F127 show that aqueous solutions above the CGT can be modelled using the Herschel-Buckley law,[44] and that high temperatures well above the CGT result in Newtonian, or viscoelastic fluids depending on the F127 concentration.[45] It has been established that at 25wt% and above CGT, F127 in water forms a normal micellar cubic phase (noted as I_1) in which the micelles crystallise in a cubic lattice.[46] This cubic phase exhibit elastic properties[47] providing a good base for printable formulations of other materials. A key benefit of Pluronic® hydrogels is that they can be used as a 'carrier' of powders with a wide range of properties, for example ceramics (oxides, and non-oxides),[18, 31, 43] carbon based materials,[4] composites,[5] and bio-inks[7, 9] among many others.

Table II. Formulation of carbon-based materials. The formulations were prepared using Pluronic F127 stock solution and GO suspensions as formulation base, and Graphite (Gr) and multi-walled carbon nanotubes (CNTs) as active carbon materials. In the hybrid formulation, GO has a dual role, as additive and active material.

FORMULATIONS	Formulation base (in distilled water)	Active Materials		
		Gr	CNTs	GO
F127	F127 (25wt%)	--	--	--
GrF127	F127 (25wt%)	38wt%	--	--
GrCNTsF127	F127 (25wt%)	38wt%	0.5wt%	--
GO	GO (5.5wt%) *(1.5vol%)*	--	--	--
GrGO	GO (1.8wt%) *(1vol%)*	31.2wt%	--	--
CNTsGO	GO (3.2 wt%) *(1.5vol%)*	--	0.5wt%	--
Hybrid	F127 (25wt%)	38wt%	0.5wt%	1wt%

F127 stock solution. A 25wt% Pluronic F127 stock solution was prepared by adding Pluronic F127 powder into a PTFE jar of distilled water at low temperature (~4 °C). Small amounts of powder were added gradually followed by a 2-minute mixing cycle at 2000 rpm in a THIARE250 planetary mixer. The mixture was cooled down in between cycles to prevent

heating during mixing and the subsequent water evaporation, in either a refrigerator or ice bath. The process was repeated until a smooth and transparent gel at room temperature was achieved. The stock solution was stored in the refrigerator at ~4°C .

***F127-active materials formulations*.** Graphite (Gr) powder was first sieved below 102μm to remove agglomerates and discard large particles that could clog the nozzle or interfere in the LAOS experiments. The Gr powders (concentrations given in table II) were added in several steps to the Pluronic F127 stock solution in a PTFE container that was kept cooled in a refrigerator at ~4°C. After a small amount of powder was added to the Pluronic stock solution, the PTFE container was sealed and mixed for 2 minutes in the planetary mixer at 2000 rpm. After each mixing cycle, the mixture was then cooled in a refrigerator or an ice bath. The formulations were subjected to at least 2 de-foaming cycles in the mixer for 2 minutes at 2000 rpm to remove air bubbles. The formulation, GrCNTsF127, that contains both Gr and CNTs, was prepared first by adding carbon nanotubes into Pluronic F127 in the cooled liquid state in a PTFE jar, following the same process as for GrF127 for several cycles until the mixture was homogeneous. Gr powders were then added following the same method as above.

Suspensions of 2D colloids as formulation base. 2D materials suspensions are a new class of soft matter in between macromolecules and colloids; this is due to their large aspect ratio and their surface chemistry (e.g. distribution of different functional groups on the basal plane and edges of the flakes). 2D GO flakes are a few atoms thick but can have a lateral flake size up to hundreds of microns, while the combination of un-oxidised hydrophobic islands and oxygen functional groups (carboxyl -*COOH*, hydroxyl -*OH*) on the basal plane and edges results in an amphiphile behaviour, enabling the establishment of a combination of inter-particle interactions (π-π stacking) and hydrogen bonds with other materials.[48] GO flakes suspensions in water form networks and gels that exhibit good printing behaviour at relatively low concentrations,[27] and can also be used as the only additive in printable formulations of oxide and non-oxide ceramics, polymers and even steel.[22] This is due to the unique combination of chemistry and morphology that GO has, an amphiphile (surfactant) 2D colloid that can establish networks through *π-π* stacking and hydrogen bonding,[48] thus able to establish interactions with a wide range of particles with different properties. Here we use GO as the only additive to prepare formulations for DIW (table II) containing graphite particles (GrGO), multiwalled carbon nanotubes (CNTsGO), and a hybrid formulation prepared with a combination of active materials and additives (hybrid).

GO stock solution (1.5vol%) was prepared by gradually adding freeze dried GO powder into the commercial GO suspension, followed by mixing in a THIARE250 planetary mixer for 2 minutes at 2000rpm.

***GO-active materials formulations*.** The graphite/graphene oxide and CNTs/graphene oxide (GrGO and CNTsGO, table II) inks were prepared using GO suspensions with concentrations of 1vol% and 1.5vol% respectively. When using the stock GO solution (1.5vol%) as a formulation base for Gr powders, the texture became lumpy and heterogenous. The best formulation was achieved using only 1vol% GO (table II). Sieved graphite powder was then added gradually in a stepwise manner followed by mixing for 1 minute in the mixer and left to cool down between mixing cycles. The formulations were also subjected to at least 2 de-foaming (which is a specific setting of the planetary mixer) cycles for 2 minutes using the THIARE250 mixer.

Large amplitude oscillatory shear (LAOS) measurements. Rheology data were collected on an ARES G2 strain-controlled rheometer (TA Instruments) using a 1mm gap, a 40mm stainless steel serrated parallel plate and a solvent trap. Amplitude sweeps were performed

on the samples at strain values that ranged between 0.01 and 250% at a fixed frequency of 0.5Hz. This range was adjusted for each specific formulation (*Materials and Methodologies* section in supporting information). These settings were chosen to probe the structure of the samples from Small to Large Amplitude Oscillatory Shear (SAOS to LAOS). LAOS tests were performed in correlation (logarithmic sweep, with 20 points per decade) and transient mode (1024 points per cycle, 3 s delay time, 6 half cycles). The correlation tests were repeated three times for all the samples in this work. Average values and standard deviation were calculated to validate our analysis from transient data. The transient data collection can be easily set up in the Trios, TA's software, and provides the raw data (strain, $\gamma(t)$ (input) and stress, $\sigma(t)$).

Data signals processing and analysis. Fourier transform (FT) rheology enables quantifying nonlinearities in LAOS tests. For a sinusoidal stress input, $\gamma(t) = \gamma_0 sin(\omega t)$, the total stress response ('whole wave approach') can be represented by a Fourier series (eq. 1) including only odd harmonics due to the assumption of symmetry with respect to directionality of shear strain or shear rate.[35, 38] Within the linear viscoelastic regime, the stress response will only include the first harmonic (*n*=1); G_1', G_1'' become the real (G') and imaginary part (G'') of the complex modulus $G^* = G' + iG''$. As nonlinear material responses arise at larger strain, higher harmonic contributions appear and grow in the material's stress response. These nonlinearities can be captured using the higher harmonics coefficients G_n' and G_n'', instead of just using the first harmonics information (G' and G'') provided by the software in the correlation mode.

$$\sigma(t) = \gamma_0 \sum_{n,odd} \{G_n'(\omega, \gamma_0) \sin(n\omega t) + G_n''(\omega, \gamma_0) \cos(n\omega t)\} \quad \text{(eq.1)}$$

The raw data signals (stress and strain vs time) were prepared before FT processing in Matlab by trimming from the first maximum of strain to guarantee that all the waves have the same length and include two full cycles. The trimmed data signals were analysed with the FFT function. The relative intensity for each harmonic I_n/I_1 is calculated from the FT spectrum. Here we build 3D maps showing the relative intensity of higher harmonics on the frequency space at increasing strain inputs. The projection of this 3D map on a strain-frequency plot enables to accurately determine the onset of nonlinearities.

Chebyshev coefficients. There are alternative approaches to the 'whole wave' Fourier coefficients approach to analyse LAOS tests, such as stress decomposition,[49] strain decomposition,[13, 33] and the Sequence of Physical Processes (SPP) developed by Rogers et al.[50-52] These approaches enable studying the yielding of soft materials and understanding different types of behaviours, such as the G''overshoot.[53] The SPP approach enables to discern elastic and viscous processes in the waveforms.[50-52] These other methods are valuable and useful, in particular the SPP method could elucidate the differences between printable and non-printable formulations and we will use them in the future to better understand the physical processes during the yielding transition. As a first step in our LAOS analysis, we use the mathematical framework proposed by Ewoldt et al.[36] based on Chebyshev polynomials of the first kind, that are orthogonal and exhibit symmetry about $x = 0$ (where $x = {}^{\gamma}/_{\gamma_0}$).[36] This approach enables us to carry out a physical interpretation of higher harmonics and determine quantitative measures of nonlinearities. The elastic (e_n) and viscous (v_n) Chebyshev coefficients were calculated from the Fourier coefficients obtained in our frequency analysis of the stress data signals, shown in eq. 2 and eq. 3, respectively.

$$e_n = G_n'(-1)^{(n-1)/2} \quad n: odd \quad \text{(eq. 2)}$$

$$v_n = \frac{G_n''}{\omega} \quad n: odd \quad \text{(eq. 3)}$$

These coefficients, e_n and v_n, can be positive and negative, which has different physical implications. The third harmonic is generally used and interpreted as a measure of the material's nonlinear response.[35, 36, 54] In the linear regime, ${e_3}/{e_1} \ll 1$ and ${v_3}/{v_1} \ll 1$, so $e_1 \rightarrow G_1'$ and $v_1 \rightarrow {G_1''}/{\omega}$. A positive value for e_3 represents intracycle strain stiffening of the elastic stress, while $e_3 < 0$ indicates strain softening. A positive value for v_3 corresponds to intracycle shear thickening of the viscous stress, and a negative value ($v_3 < 0$) describes shear thinning.

Elastic moduli in the nonlinear regime, G_L' and G_M', are also used as a material measure of nonlinearities and can be determined from Fourier and Chebyshev coefficients, and in principle, based on their definition from the Lissajous-Bowditch (L-B) curves (see next subsection).

$$G_M' \equiv \left.\frac{d\sigma}{d\gamma}\right|_{\gamma=0} = \sum_{n,odd} nG_n' = e_1 - 3e_3 + 5e_5 \ldots \quad \text{(eq. 4)}$$

$$G_L' \equiv \left.\frac{\sigma}{\gamma}\right|_{\gamma=\gamma_0} = \sum_{n,odd} G_n'(-1)^{{(n-1)}/{2}} = e_1 + e_3 + e_5 \ldots \quad \text{(eq. 5)}$$

When $G_L' > G_M'$, the material is strain stiffening within a given cycle, and $G_L' < G_M'$ correspond to strain softening. Continuing with the same framework by Ewoldt et al,[36] these elastic nonlinear moduli can be used to calculate a strain stiffening ratio (S), the dimensionless index of nonlinearity.[36] This strain stiffening ratio becomes 0 for a linear elastic response, $S > 0$, indicates strain stiffening and $S < 0$ strain softening.

$$S \equiv \frac{G_L' - G_M'}{G_L'} \quad \text{(eq. 6)}$$

Lissajous analysis. Material stress responses to LAOS can be visually interpretated using *Lissajous-Bowditch* (L-B) plots, in which the full stress response is plotted parametrically against the strain (elastic representation) or shear rate (viscous representation). LAOS responses can be visualized in a 3D space with the stress ($\sigma(t)$), strain ($\gamma(t)$), and strain rate ($\dot{\gamma}(t)$) as the coordinate axes (Figure S5 and S6, supporting information).[35, 38, 54] From these 3D spaces we can plot different projections, such as stress vs. strain ($\sigma(t)\ vs.\ \gamma(t)$) denoted as the *elastic L-B curves*, and stress vs. strain rate ($\sigma(t)\ vs.\ \dot{\gamma}(t)$) denoted as the *viscous L-B curves*.[38] A material with a purely elastic response forms a straight line in the elastic L-B plot, while a purely viscous response will form a circle (in a suitably scaled plot), and a viscoelastic response an ellipse in the LVR (figure 2).[38] Moderate and large viscoelastic nonlinearities can be easily identified by non-elliptical distortions in the L-B curves (figure 2).[38] These curves provide a valuable visual approach to qualitatively compare different formulations in the absence of an FT analysis (section E). The distortions of L-B curves can be analysed and quantified in different ways, such us determining the minimum (G_M') and large (G_L') higher harmonic moduli defined in equations 4 and 5. G_M', is the minimum-strain modulus, or tangent modulus at $\gamma = 0$, and G_L' is the large-strain modulus, or secant modulus at the maximum imposed strain $\gamma = \gamma_0$[36] (figure 2).

The raw data signals were smoothed (using the moving median function with a window of 20), to create Lissajous 3D spaces ($\sigma(t),\ \gamma(t),\ \dot{\gamma}(t)$,[35, 38, 54] included in the supporting information (Figures S5 and S6) for all the formulations in this work). Smoothing the raw data avoids 'kinks' in the curves plotted in the 3D space and L-B projections, that sometimes appear due to measurement noise, which becomes more noticeable when calculating the strain rate ($\dot{\gamma}(t)$) values from the raw data signals. 3D surfaces can also be analysed using the SPP method that utilizes the Frenet-Serret Theorem, which defines the position of a moving particle along

a curvature in a coordinate system with a set of vectors.[52, 55] The projection of binormal vectors is evaluated to define transient elastic (G_t') and viscous moduli (G_t'').[17, 55, 56] In this work we implement Fourier Transform coupled with Chebyshev polynomials,[36] using the material measures defined in the previous section, G_L', G_M' (figure 2). We also determine G_L', G_M' directly from the L-B curves for the F127 stock solution as an example (section D).

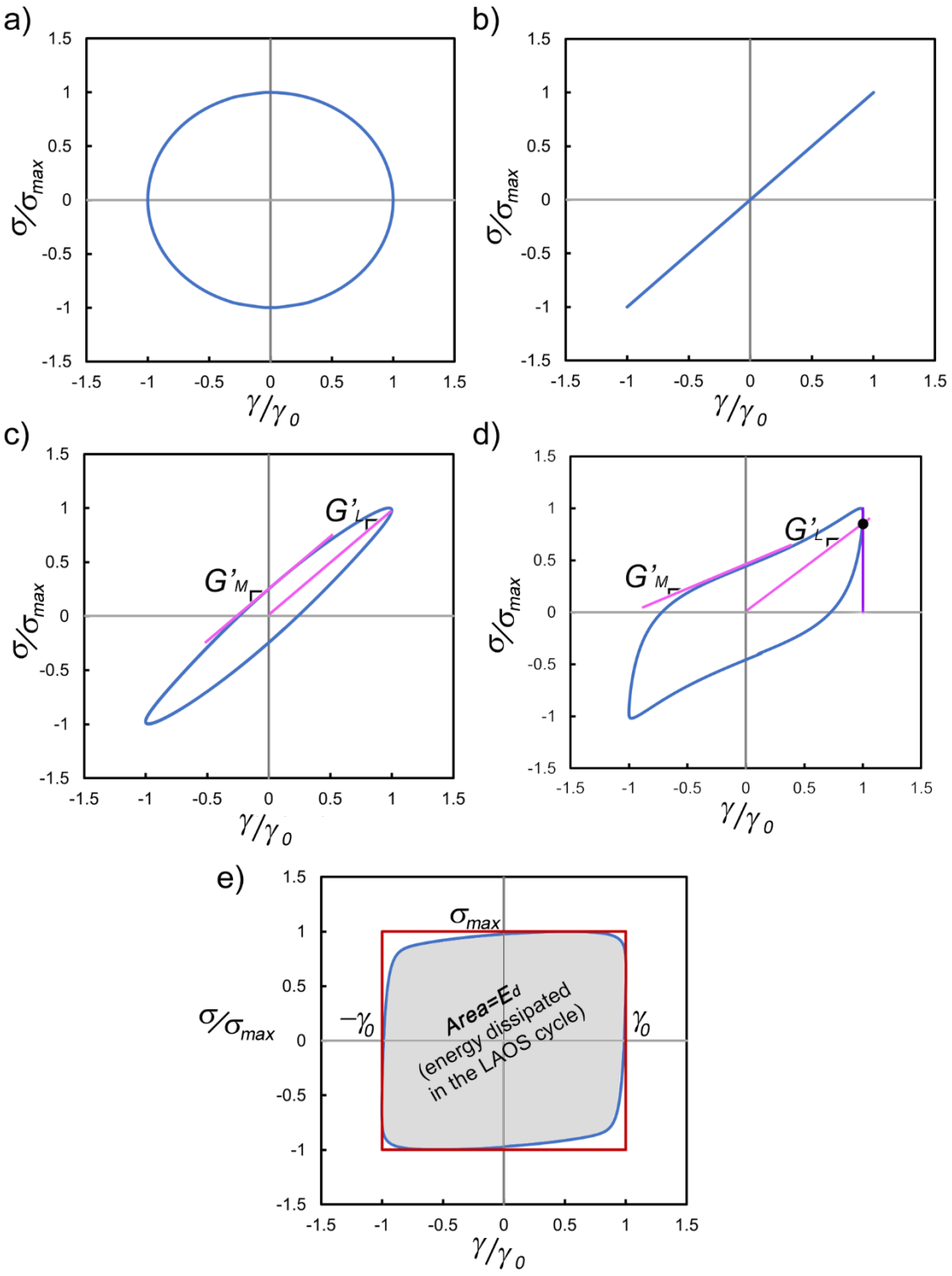

Figure 2. Lissajous-Bowditch elastic plots for: a) perfectly viscous material; b) perfectly elastic material; c) viscoelastic material in the LVR; d) viscoelastic behaviour in the nonlinear region. The plots in c) and d) show how G_M' (minimum-strain modulus, or tangent modulus at $\gamma = 0$) and G_L' (large-strain modulus, or secant modulus at the maximum imposed strain, γ_0) can be determined from the L-B plots. These visual representations also show that:

c) in the LVR $G'_M = G'_L$, and d) in the nonlinear region $G'_M < G'_L$, this is (in principle) associated with intracycle strain-stiffening behaviour. The curves in (c), (d) and (e) are schematic to explain typical L-B plots and calculation of different parameters; they do not represent the data obtained from our experiments.

Yield stress fluids such as drilling fluids exhibit similar *n* (flow index) values to DIW formulations (*n*=0.099 for an invert-emulsion drilling fluids[38]; n→0 for printable GO suspensions[27]) albeit the latter have larger storage modulus in the LVR (G'_1 in the range of kPa to GPa). Some of the material measures that can be determined from the LAOS and FT analysis for this type of complex fluids are sensitive to the data acquisition rate, resulting in larger slopes at discontinuities.[38] The fact that the rate of deformations is not constant within a given cycle[57] can lead to a *"strain softening/strain hardening paradox"*[57] and discrepancies between different methodologies (section D).

A material measure that has almost no sensitivity to the data acquisition rate is the perfect dissipation ratio, ϕ, which is a metric to quantify how closely a particular LAOS response is to an idealised perfect plastic yield stress behaviour.[38] This type of ideal behaviour corresponds to microstructures like the DIW formulations in this work that are disrupted by certain yield stress (unique for each formulation), but that after disruption easily flow. ϕ compares the energy dissipated in a single LAOS cycle (area enclosed in a Lissajous curve, in grey in figure 2e, $E_d = \oint \sigma d\gamma$) to the energy that would be dissipated in a rigid, perfect plastic response with equivalent strain amplitude γ_0, and maximum stress σ_{max} (area delimited by the red square in figure 2e, $(E_d)_{pp} = (2\gamma_0)(2\sigma_{max})$).[38] The energy dissipated in a LAOS cycle can also be calculated using the first-order viscous Fourier coefficient, thus ϕ can be calculated using equation 7.[38]

$$\phi \equiv \frac{E_d}{(E_d)_{pp}} = \frac{\pi \gamma_0 G_1''}{4\sigma_{max}} \qquad \text{(eq. 7)}$$

This measure is described as "well-behaved" for any arbitrary LAOS response because the strain amplitude and maximum stress are always well-defined and easily determined from the data. A perfect plastic behaviour corresponds to $\phi \to 1$, a purely elastic response to $\phi \to 0$, and $\phi \to {}^{\pi}/_{4} \approx 0.785$ corresponds to a Newtonian behaviour.[38] This measure is used in this work to compare the behaviour of different DIW formulations in section E.

III. RESULTS AND DISCUSSION

A. Printability of carbon-based formulations for DIW

We have previously reported a protocol to determine the 'printability' of soft materials[27] using GO suspensions with different concentrations that exhibit a wide range of behaviours from nearly Newtonian to 'printable'. What we mean – and it is generally understood within the DIW community – when we label a formulation as 'printable' is that we can reproduce the 3D shape that we originally designed based on a visual judgement of print quality. We also mean that during the printing of the part: 1) the formulation flows steadily without showing dye swell effects, clogging the nozzle, showing signs of phase separation, filter press effects, or segregation; 2) that the filament retains its shape; and 3) that the final part can support its own weight without deformation, slumping or collapsing. It is possible to assess the 'printability' of a formulation by empirically observing its performance during printing, however we do not recommend this unscientific approach to characterise and classify complex fluids for DIW.

Using this preliminary and empirical assessment (summarised in table III), we found that the GrGO formulation in this work, is not printable (table III). When using the syringe pumps, this

formulation does not steadily flow through the tip of the nozzle. Instead, its microstructure is disrupted under the plunger displacement, resulting in 'filter-press' effects and water segregation. We must admit that we did not expect this result, as we had successfully formulated different materials using GO as the only additive.[22] We hypothesise the factors that are causing this behaviour are: 1) using GO from a commercial source with relatively small lateral flake size (see materials and methods section); 2) combined with graphite particles that are relatively large compared to the GO flake lateral size; and possibly, but not as relevant based on WCA measurements, 3) that the GO elemental analysis shows a lower C/O ratio. It has been reported that the larger the lateral flake size, the lower concentration is needed to form a printable gel.[42] Factors 1 and 2 are highly likely limiting the ability of (small) GO flakes to form a network with (large) Gr particles that can break down and rebuild with ease. However, this unexpected result offers an excellent opportunity to compare this formulation with printable ones in this study, and to explain its poor performance from a rheology perspective (in sections III.B to E). It has not been possible to formulate a printable formulation with both active materials (Gr and CNTs), however we have been able to do so combining CNTs and GO in the absence of Gr particles. Active materials are added in different amounts with the purpose of increasing functional performance, in this case, electrical conductivity. Gr particles, with large average size and low specific surface area (table I), are added in large amounts to formulate conductive pastes using F127 and GO as additives (table II). On the other hand, CNTs, with dimensions in the nm scale, large surface area and large aspect ratio (table I) are added in very small amounts (table II) to improve functional performance.[34] CNTs added in such small amounts can easily create conductive pathways and improve electrical conductivity.[34, 58, 59] The intrinsic properties of the active materials and additives play a critical role in the microstructure, network formation and rebuilt, and therefore on their 'printability'. The failure of the GrGO formulation could be explained by a lack of network formation between GO and Gr particles, due to weak, or lack of, inter-particle interactions. In short, the small GO flakes from a commercial source are not a suitable approach to prepare printable GrGO formulations, but they can be successfully used to aid the printing of CNTs, and hybrid formulations (table III). The hybrid performs well during printing, which suggests that the combination of F127 and GO, do enable the formation of a network between the Gr particles and CNTs, that can be broken and rebuilt to meet DIW demands.

Table III. Summary of the printability of carbon-based formulations for DIW. The GrGO formulation is the only not printable formulation in this study. All the other inks easily yield and flow when sheared due to the plunger displacement in the syringe pump. They form a filament when exiting the tip of the nozzle, and retain the shape once deposited on the substrate.

Formulation	F127	GrF127	GrCNTsF127	GO	GrGO	CNTsGO	Hybrid
Printable Y/N	Y	Y	Y	Y	N	Y	Y

B. Fourier transform (FT) rheology analysis

The sequence of strain input waves through the amplitude sweep (as γ_0 increases) and the sequence of the material's stress responses are shown in figure 3. The highlighted region shows a full cycle in the amplitude sweep (from $\gamma = 0$ all the way to γ_0, back to 0 and then backwards to $-\gamma_0$ and back to $\gamma = 0$). These strain input waves are perfectly sinusoidal and do not show any distortion. We have also validated the quality of the input strain waves by checking their spectra, where we observed only one dominant frequency (corresponding to the oscillation frequency, ω_0) for all the strain amplitudes. Figure 3b shows the material's response, a sequence of stress data signals. As the strain increases in the sweep so does the

stress, however as γ_0 increases over certain values, the stress waves start showing distortions (highlighted by the arrows in figure 3b). These distortions can be represented in the form of higher order ($n \geq 3$) harmonics.[36] Figure 3c shows the FT results for F127 stock solution as a representative example. This 3D map shows the intensities of higher harmonics with respect to the intensity of the 1st harmonic (I_n/I_1, z-axis) *vs* both the frequency (with ticks and labels for the odd harmonics in the x-axis, odd multiples of $\omega_0 = 0.5\,Hz$) and γ_0 (strain amplitude) values on the y-axis. The 3D maps compile all the FT spectra and provide a visual 'snapshot' of the onset and growth of higher harmonics as γ_0 increases. The stress data signals and FT 3D maps for all the formulations in this work are included in the supporting information (Figures S1 to S4). Distortions on the stress waveforms become evident for all the formulations as strain increases due to the contribution of higher harmonics. The best way to determine the precise onset of non-linearities for each higher harmonic is using the *x-y* projection FT fingerprints (figure 4), plotting the strain γ_0(%) on the *y-axis*, *vs* the FT frequency ($n \cdot \omega_0$) on the *x-axis* with labels for the n harmonics. FT fingerprints for all the samples in this work are compared in figure 4, and the main results from this analysis are compiled in table IV.

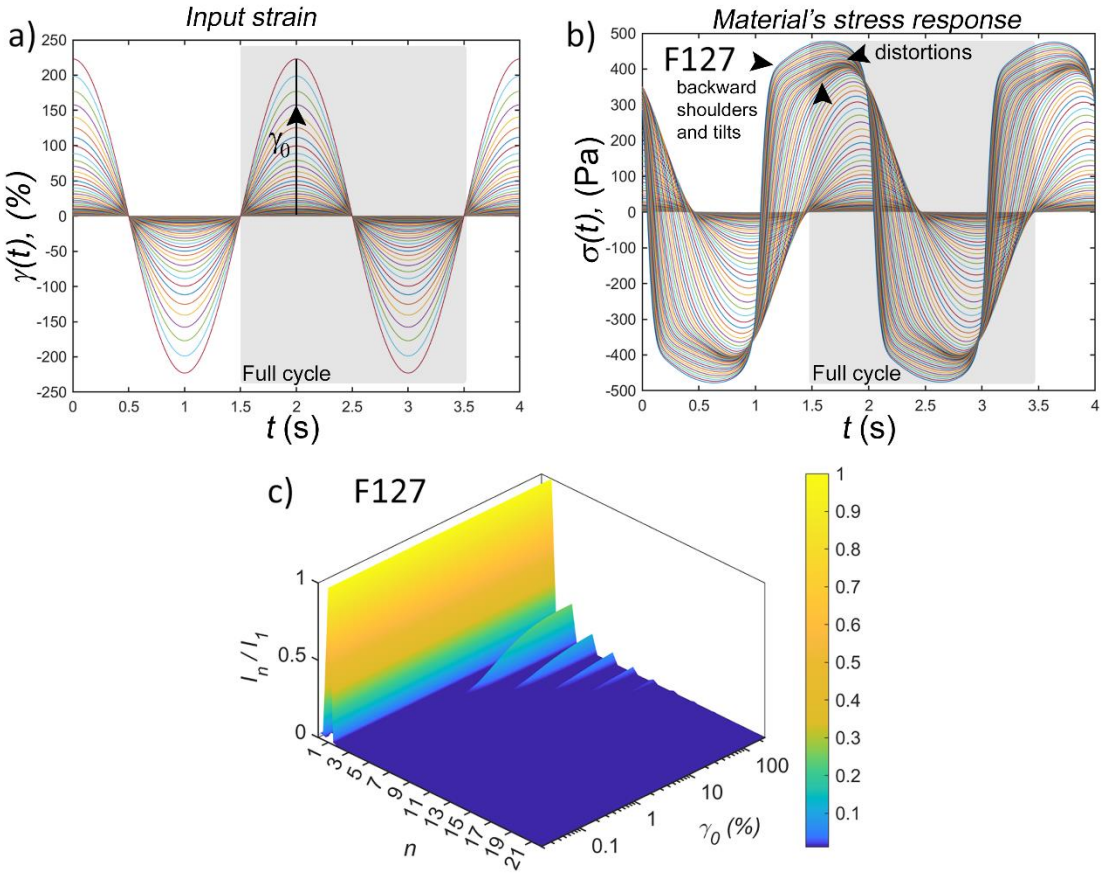

Figure 3. FT analysis for the F127 stock solutions used as formulation based in this work. (a) Sequence of the strain input waves for all the datapoints in the sweep. The waves are shown after the trimming process from the first maximum of strain; (b) Material's response: sequence of stress waveforms after trimming. The stress waveforms for F127 show backward shoulder tilts (black arrows) and features that suggest a behaviour between "soft" and "hard" gel.[40, 60] (c) 3D FT harmonics maps showing the relative intensity of odd harmonics (I_n/I_1) for F127.

The FT analysis shows quantifiable differences between the two formulation additives used in this work, F127 and GO. The FT analysis also enables us to quantify the impact of the addition of active materials, Gr and CNTs. LAOS tests of DIW formulations often show a narrow LVR region, which makes its limits extremely subjective. The FT analysis provides a quantitative determination of the LVR limits and therefore, of the yielding transition. In this study, only the

intensities of harmonics which are more than 1% of the intensity of the first harmonic (I_1) is considered for the FT analysis, and anything below $0.01I_1$ is considered as noise. The onset of nonlinearities (NL) is determined when $I_3/I_1 > I_{noise}{\sim}0.01$, and takes place at $\gamma_0 \approx 2.8\%$ for F127 and $\gamma_0 \approx 0.9\%$ for GO (table IV, figure 4). The addition of Gr particles to the F127 hydrogel matrix triggers an early onset of the third harmonic at $\gamma_0 \approx 0.04\%$ (figure 4). However, CNTs added in small amounts to increase the electrical conductivity[34] to this GrF127 formulation do not seem to change the FT spectra, or the onset of nonlinearities (figure 4, and table IV). The impact of the CNTs addition is negligible compared with the intense effect that highly concentrated Gr particles in the F127 matrix have. When using GO as formulation additive, the FT map for GrGO (not printable, table III) shows the onset of the third harmonic at small strain values, $\gamma_0 \approx 0.11\%$ (figure 4b, table IV), however this result does not flag any distinctive feature that could be associated with 'printability' or lack of, from these FT fingerprints. The FT maps for CNTsGO and GO are very similar (both in figure 4b). Although the onset of the third harmonic takes place at slightly smaller γ_0 for CNTsGO (table IV), evidencing that the addition of a small amount of CNTs to GO does not have a big impact on the GO network microstructure. The hybrid formulation containing all additives and active materials (Gr, CNTs, GO and F127) has an excellent printing behaviour (table III), and very interesting functionality when subjected at different post-processing conditions.[34] The FT harmonics fingerprint for this hybrid (figure 4) is similar to those for GrF127 and GrCNTsF127. The onset of nonlinearities takes place at $\gamma_0 \approx 0.045\%$ (figure 4, table IV).

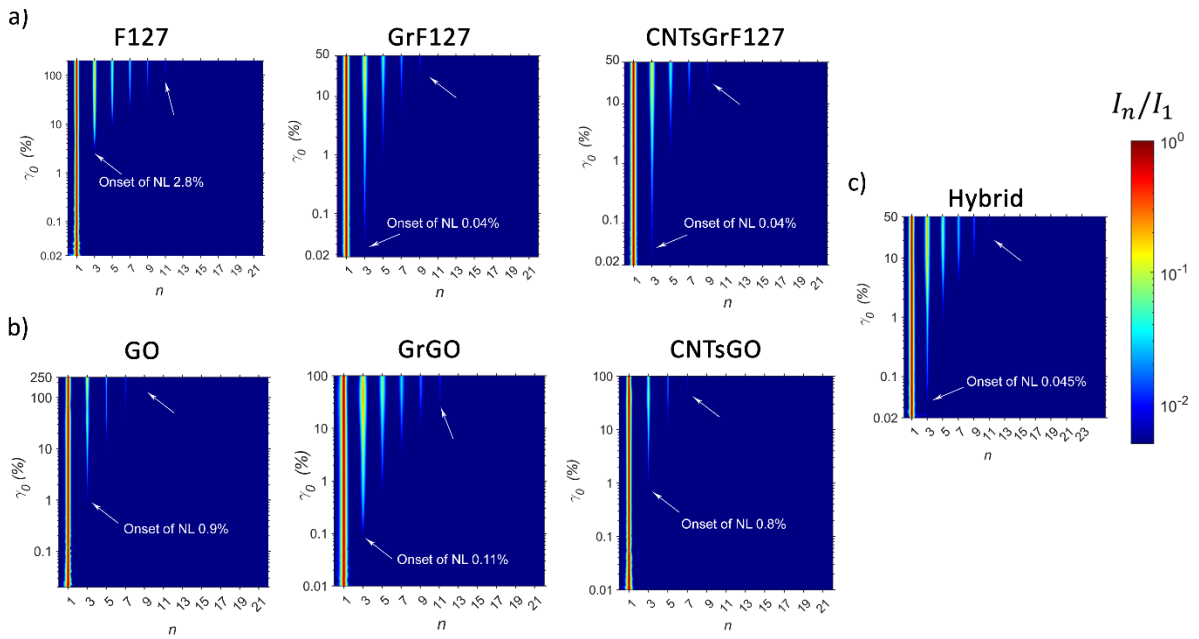

Figure 4. FT analyses comparison for all the samples in this work using the strain-frequency projections (γ_0(%) *vs.* ($n \cdot \omega_0$) plots) obtained from the 3D harmonics (I_n/I_1) maps for: a) F127 formulations (F127, GrF127 and CNTsGrF127); b) GO formulations (GO, GrGO and CNTsGO); and c) Hybrid formulation. The 3D FT maps are included in figure 3 (F217) and in the supporting information: figures S1 (GO), S2 (GrF127 and CNTsGrF127), S3 (GrGO and CNTsGO) and S5 (Hybrid). The legend for all the contour maps is included on the right. These projections enable us to precisely determine the onset of nonlinearities (γ_{NL}(%)) when $I_3/I_1 > I_{noise}{\sim}0.01$. They also show the number of higher harmonics for which $I_n/I_1 > 0.01$ is satisfied for each sample (indicated with arrows in the maps).

3D FT harmonics maps provide a useful visual interpretation of the onset and rising of nonlinearities, and the relative intensity of the different harmonics. The 2D FT fingerprints enable us to accurately determine the limits of the LVR, and the start of the yielding transition, which is a very important measure in DIW. The FT analysis results demonstrates that LAOS and FT rheology are a powerful tool to quantify the contribution of each active material and

additive on nonlinear behaviours. Even if a direct link between such nonlinear behaviours and 'printability' does not emerge yet from our results, we can already assert that the FT analysis will help us optimise the synthesis of bespoke additives (such as pH-responsive branched copolymer surfactants)[3] and formulation design.

C. LAOS analysis: first harmonic moduli and stress-strain curves from dynamic strain sweeps

The first harmonic moduli, G_1' and G_1'', calculated from the Fourier coefficients from transient data, or those given by the rheometer's software (figure 5), enable us to classify the behaviour of the formulations. For the F127 and GO formulations we include a comparison between the first harmonic moduli values obtained from our transient data signals FT analyses (figure 5), with the average and standard deviation from three amplitude sweeps performed in correlation (calculated by *TRIOS* software). The results show an excellent agreement (figure 5), and for simplicity we omit this comparison for the other formulations.

Plotting the recast of first harmonic moduli (figure 5a), and the stress *vs.* strain data on a separate plot (figure 5b), help us to compare the yielding transition of our formulations. These stress-strain graphs are inspired by a previous study that correlates LAOS and steady shear of soft solids.[37] Note that we do not include any steady shear experiments here because the results for our printable formulations are considerably uncertain.[27] In the stress-strain plots we include the following rheological parameters for the analysis: $\gamma_C(\%)$ is the critical strain (determined at the cross-over point $G_1' = G_1''$ (figure 5a, c)); and $\gamma_{NL}(\%)$ is the strain at the onset of nonlinearities determined from the $\gamma_0(\%)$ *vs*. $(n \cdot \omega_0)$ plots, *x-y* projections of the 3D FT harmonics maps (figure 4, table IV). We show that the start of the yielding transition takes place at the onset of nonlinearities ($\gamma_{NL}(\%)$, $\sigma_y(Pa)$, table IV); from this point the slope of the stress *vs*. strain plot starts to change, and plateaus around the critical strain (figure 5b, d). We consider this 'plateau' on the stress values as the "bulk flow" stress, noted as $\sigma_f(Pa)$. The extent of the yielding transition is delimited between $\gamma_{NL}(\%)$ and $\gamma_c(\%)$. Here we also provide a comparison of the $\gamma_{NL}(\%)$ and $\sigma_y(Pa)$ values obtained through the quantitative FT approach (table V) with the values that would be obtained in its absence by using the following approaches: 1) considering the end of the LVR when $G_1' < 0.90G_{LVR}'$, or when $G_1' < 0.95G_{LVR}'$ (this is the most commonly used method in DIW); and 2) when a change of slope is observed in the stress amplitude vs stress amplitude log-log plot (figure 5b, d).

F127 stock solution shows a type III behaviour (weak strain overshoot, figure 5a), while the GO formulation shows a type I behaviour (strain thinning, figure 5c).[61] Type III behaviour has been reported for other plastic soft materials, Carbopol, Xanthan Gum and concentrated Ludox also display this behaviour.[53] This very recent work based on strain decomposition investigates plasticity and the yielding transition to differentiate between two modes of dissipation (solid-like and liquid-like),[53] the overshoot in the loss modulus is related to plasticity and a gradual yielding transition. This yielding transition is key in DIW, and it is directly related to printability. Our research and experience provide evidence demonstrating that printable formulations are complex fluids type I or type III,[61] however we do not yet see a direct correlation between type III and printability. Both formulation base systems, F127 and GO, are printable and exhibit similar values of G_1' and G_1'' in the linear regime (~10,000 Pa), and both show a strain thinning behaviour in the nonlinear regime. However, there are also clear differences between them: the linear regime for GO is narrower; F127 shows a loss modulus overshoot; and they exhibit a clearly different critical strain $\gamma_c(\%)$ (figure 5a, c). The stress-strain plots (figure 5b, d) shows that both, F127 and GO, follow a similar trend with slightly different stress values (table IV). Both show a clear stress plateau (figure 5b, d) with differences in their yielding region, which is very narrow for F127.

The values for $\gamma_{NL}(\%)$ and $\sigma_y(Pa)$ obtained using different methods (table V) demonstrate that the most accurate and objective approach to determine the onset of nonlinear behaviour (and therefore the limit of the LVR) is using the FT analysis. In the absence of an FT analysis, the change in the slope of the stress vs strain log-log plot (figure 5b, and d) is the approach that leads to less errors in the determining $\gamma_{NL}(\%)$ and $\sigma_y(Pa)$. The commonly used approach based on $G_1' \leq$ 0.95G'_{LVR} or 0.90G'_{LVR} underestimates the σ_y values (table V). A lack of consistency in these methodologies within the DIW field might unfortunately lead to unreliable metrics based on these values. We defined the flow transition index (dimensionless parameter, $FTI = {}^{\sigma_f}/_{\sigma_y}$) as the ratio between the stress plateau, or bulk flow stress, divided by the stress value at the onset of the yielding transition.[27] We found that GO formulations become printable at concentrations that results in FTI < 20.[27] All the formulations in this work meet this requirement (table IV), however this dimensionless parameter by itself is not enough to guarantee the printability of a formulation, and we advise that other aspects must be considered, such as the magnitude of the storage modulus in the linear regime and the flow stress. This is explained in more detail in section III.F.

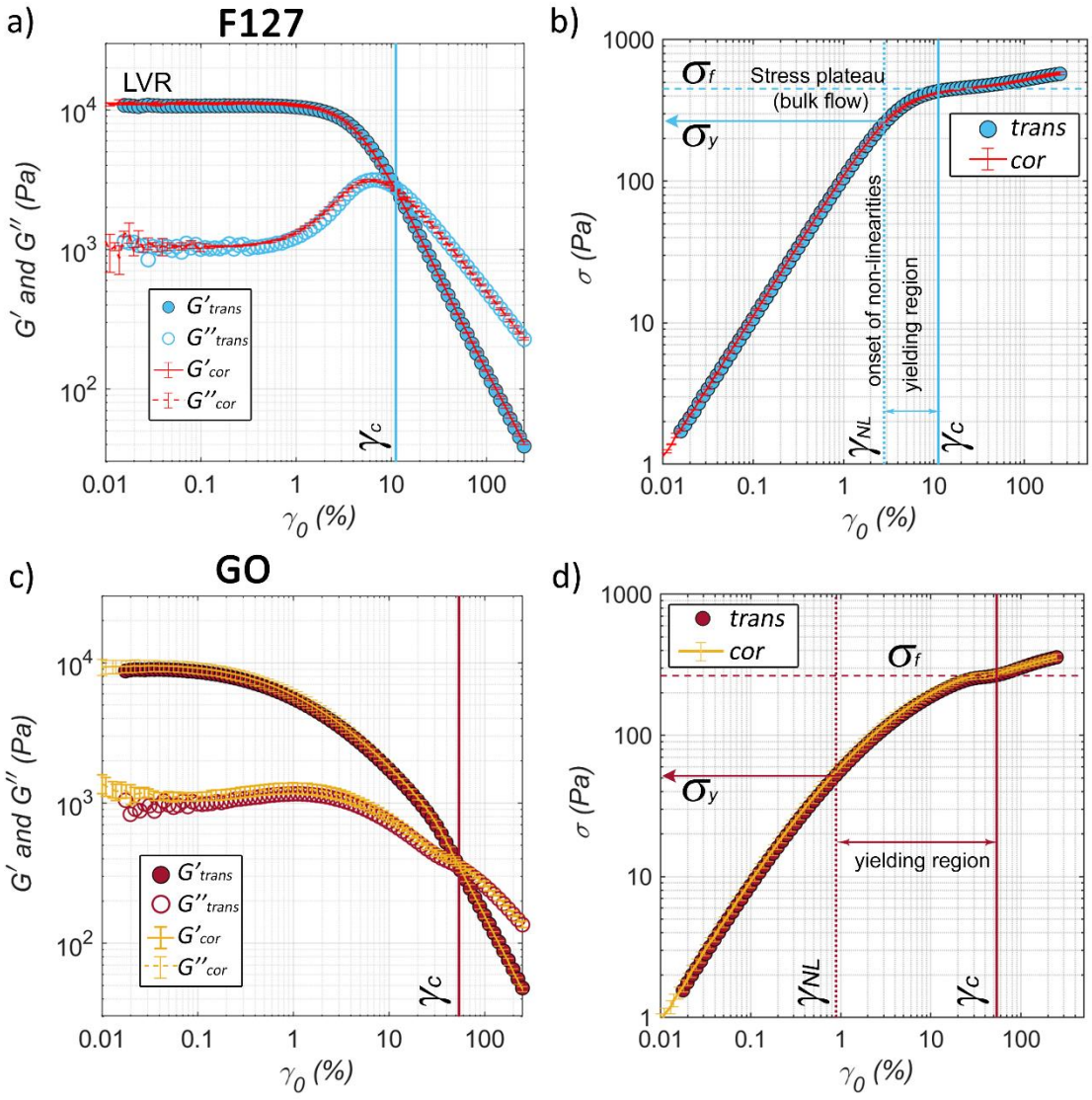

Figure 5. Validation of our analysis comparing the results from transient (from Fourier coefficients) vs correlation data (*TRIOS* software) for F127 (a, b) and GO (c, d) stock solutions. (a, c) First harmonic moduli G_1' (Pa) and G_1'' (Pa) obtained from the rheometer's software (average and standard deviation of 3 repeats in correlation (*cor*) data collection) compared with those calculated from the Fourier coefficients (transient, *trans*). (b, d) Stress amplitude vs strain amplitude from correlation (*cor*) and transient (*trans*) results.

F127 formulations. When active materials (Gr and CNTs powders) are added to F127 stock solution, the behaviour shifts from type III (weak strain overshoot) to type I (strain thinning) (figure 6). The linear regime becomes considerably narrower for both, with an onset of nonlinearities at $\gamma_0(\%) = 0.04$; the storage modulus increases one order of magnitude (up to ~140,000 Pa); the critical strain, $\gamma_c(\%)$, drops from 11.2 for F127 to 7 for GrCNTsF127; both, $\sigma_y(Pa)$ and $\sigma_f(Pa)$ increase, however the increase of the yield stress $\sigma_y(Pa)$ is more notable (table IV, figure 6b). The extent of the yielding region (for 'filled' F127 with active materials) is considerably larger in terms of strain range, but the FTI values are still below 20.

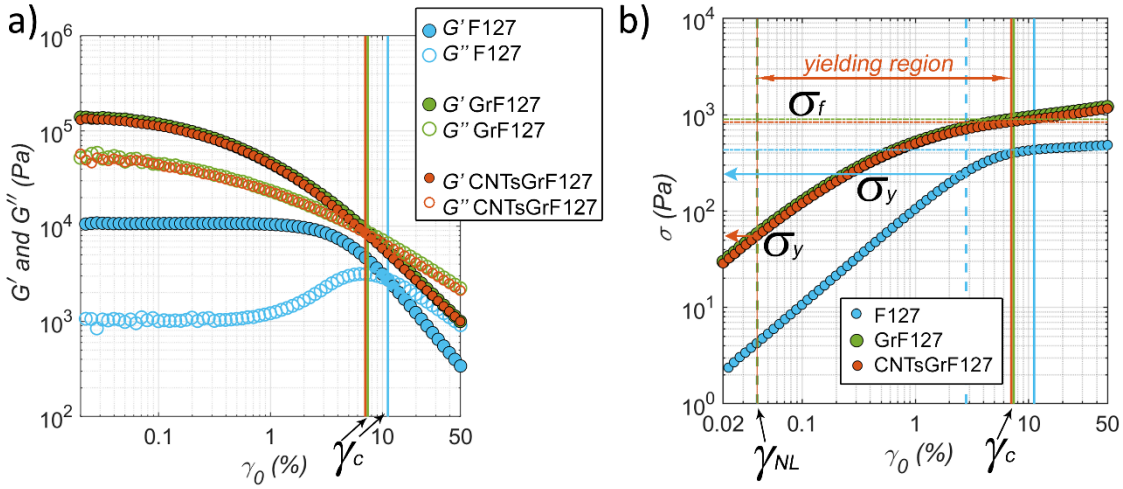

Figure 6. Comparison of F127-based formulations. (a) First harmonic moduli $G_1'(Pa)$ and $G_1''(Pa)$ calculated from the Fourier coefficients, and (b) stress amplitude vs strain amplitude from transient results for pure F127 and two F127 formulations: GrF127 and GrCNTsF127. Both formulations exhibit almost identical results that are clearly different to pure F127. The addition of active materials shifts the behaviour from type III to type I.

GO formulations. When adding active materials (Gr and CNTs powders) to the GO stock solution, two different responses have been observed. *CNTsGO formulation.* The addition of CNTs to GO slightly changes the values of $G_1', G_1'', \gamma_{NL}(\%), \gamma_c(\%)$, $\sigma_y(Pa)$ and $\sigma_f(Pa)$ but their behaviour is very similar (table IV, figure 7). Both, GO and CNTsGO, exhibit type I behaviour,[61] similar yielding transition, critical strains and plateaus in the stress-strain curve (figure 7). *GrGO formulation.* The addition of Gr powders to GO results in a formulation that is not printable (see section III.A). The formulation is very stiff, with G_1' values of >1MPa (table IV) and although it also shows a strain thinning behaviour (type I), the critical strain $\gamma_c(\%)$ at the cross-over point (G_1', G_1'') takes place at an even larger strain than GO (~80 %, table IV, figure 7b). The stress-strain curve shows that the stress values for GrGO are considerably higher than for any other formulation (figure 7b, c) with a stress value at the start of the yielding transition of $\sigma_y(Pa)$~ 463 (table IV). The extent of the yielding transition also increases due to the onset of nonlinearities at small strains ($\gamma_{NL}(\%) = 0.11$), and the increase of the critical strain ($\gamma_c(\%) = 80$). Worth noting is the unusual (different to all the other printable samples) stress-strain curve for GrGO (figure 7c). It shows a maximum in the MAOS region ($\sigma_{max}(Pa)$~ 2500; $\gamma_{max}(\%)$~3%) at much smaller strains than the critical for this formulation ($\gamma_c(\%) = 80$). This extreme behaviour can be clearly seen in figure 7c; the stress-strain curve shows a maximum and then drops to a minimum before increasing again at the critical strain. There is not a plateau on stress values that can be correlated with bulk flow. The fact that such a large value of stress is reached at low strain to then drop considerably could be related to slip, shear banding, sample fracture, or microstructure disruption. We cannot confirm or quantify these potential issues, but we can assert that this formulation does not display a smooth yielding transition unlike the other printable samples. Experimental evidence during the printing tests (section III.A) suggests that the microstructure becomes disrupted under

stress resulting in water segregation at the tip of the nozzle due to filter-press effects; the nozzle gets clogged due to the aggregation of graphite/GO particles that separate from the water.

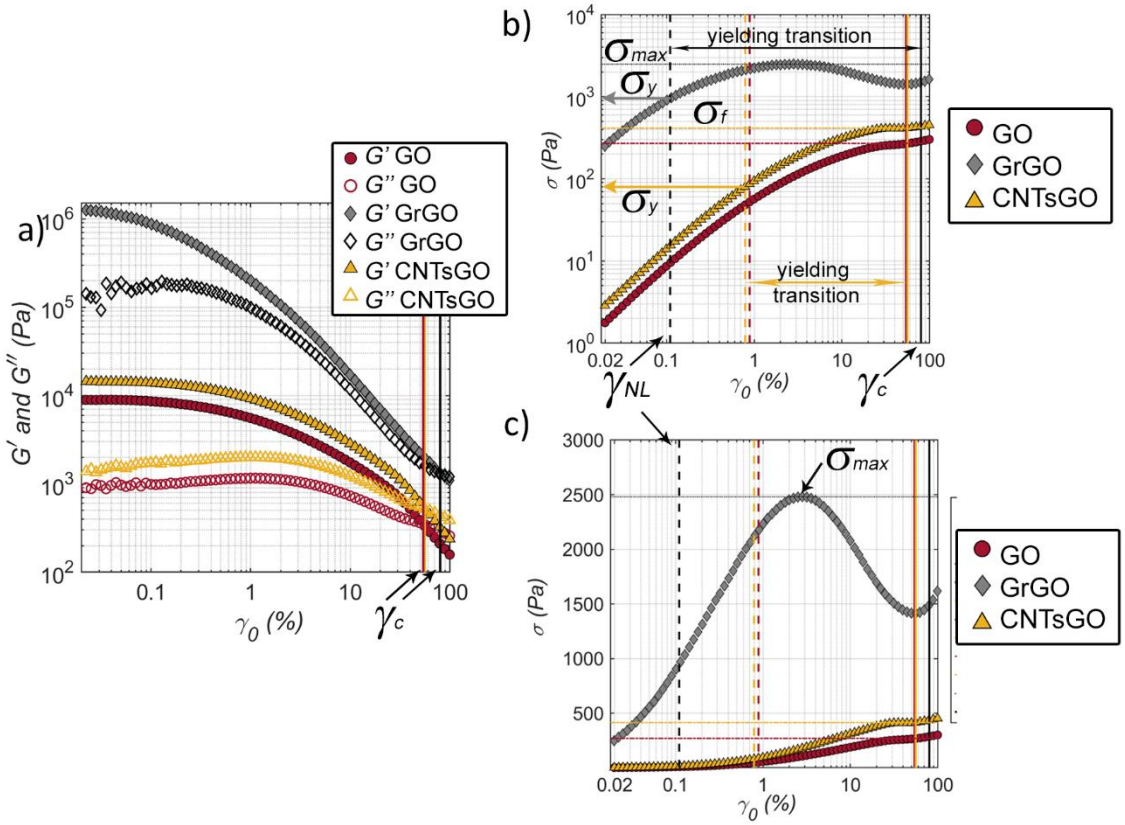

Figure 7. Comparison of formulations using GO as the only additive. (a) First harmonic moduli $G_1'\ (Pa)$ and $G_1''\ (Pa)$ calculated from the Fourier coefficients, and (b) stress amplitude vs strain amplitude (log-log plot) from transient results for pure GO and two carbon-GO formulations: GrGO and CNTsGO. (c) Stress-strain semi-log plot showing the extreme behaviour for the GrGO formulation.

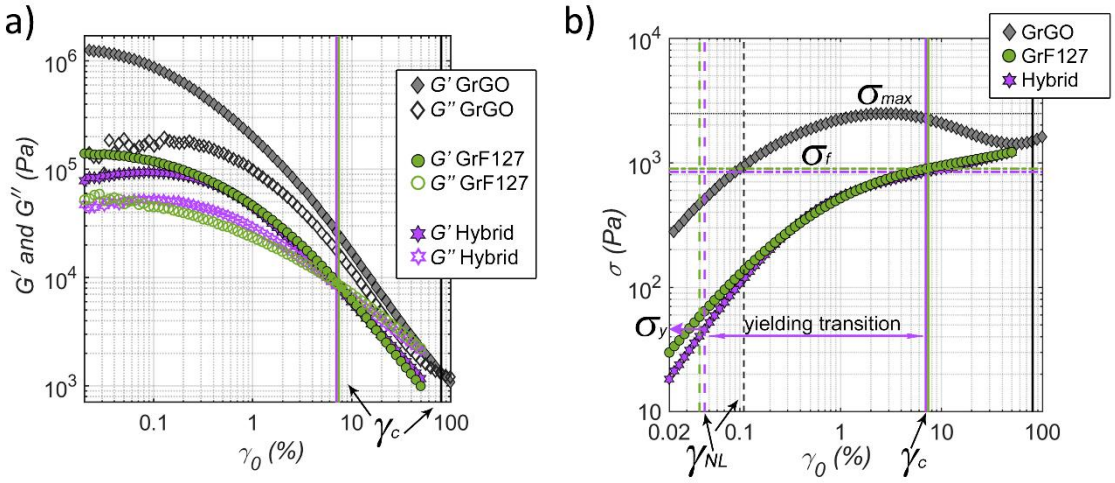

Figure 8. Comparison of Gr formulations. (a) First harmonic moduli $G_1'\ (Pa)$ and $G_1''\ (Pa)$ calculated from the Fourier coefficients, and (b) $\sigma(Pa)$ (stress amplitude) vs γ_0 (strain amplitude) in a log-log plot from transient results for all the formulations that contain graphite: GrF127, GrGO and hybrid (GrCNTsGOF127). Vertical dashed lines in the graphs represent the onset of nonlinearities ($\gamma_{NL}(\%)$) determined from the FT harmonic maps (figure 4, section

III.B). Solid vertical lines in the graphs represent the critical strain values ($\gamma_c(\%)$) determined from the crossover of the first harmonic moduli (section III.C).

Comparison of Gr formulations. The hybrid formulation containing both additives (F127 and GO) and active materials (Gr and CNTs), shows a very similar behaviour to GrF127 (figure 8). This network shows a smooth yielding transition unlike the GrGO formulation (figure 8b). The hybrid exhibits very similar $\gamma_c(\%)$ $\gamma_{NL}(\%)$, $\sigma_y(Pa)$ and $\sigma_f(Pa)$ values, and yielding transition compared to those for the GrF127 formulation (table IV, figure 8). These results evidence that the Gr particles and the F127 matrix make the strongest contribution to the rheology of the combined formulation. Although the GO flakes and CNTs in the hybrid formulation do not seem to substantially change the rheological behaviour, they do play an important role from a functional perspective.

Table IV. FT rheology and LAOS results for F127, GO and carbon-based formulations. In the third column, $\gamma_{0\,max}$ indicates the maximum value of the strain amplitude studied for each sample and n indicates the maximum value of the harmonic for which $I_n/I_1 > 0.01$ is satisfied.

FORMULATIONS	FT analysis		LAOS results				
	Onset of NL,γ_{NL} (%)	Higher harmonics, *n*, at $\gamma_{0\,max}$	σ_y(Pa) *(Onset of NL)*	γ_c (%)	σ_f(Pa) *(Bulk flow)*	G_1'(Pa) *(Linear regime)*	*FTI* σ_f/σ_y
F127	2.8	11th ($\gamma_{0\,max}$= 250%)	257	11.2	450	11,000	~2
GO	0.9	9th ($\gamma_{0\,max}$= 250%)	52	54	270	9,000	~5
GrF127	0.04	9th ($\gamma_{0\,max}$= 50%)	58	7.4	890	140,000	~15
GrCNTsF127	0.045	9th ($\gamma_{0\,max}$= 50%)	55	7	840	135,000	~15
***GrGO**	0.11	11th ($\gamma_{0\,max}$= 100%)	463	80	--	1,250,000	--
CNTsGO	0.8	7th ($\gamma_{0\,max}$= 100%)	80	56	410	14,000	~5
Hybrid	0.045	11th ($\gamma_{0\,max}$= 50%)	46	7	840	90,000	~18

**Not printable. This formulation exhibits a max stress (σ_{max}~2500 Pa) in the MAOS region before the solid-to-liquid transition, and therefore a bulk flow plateau cannot be determined.*

Table V. Comparison of $\gamma_{NL}(\%)$ and $\sigma_y(Pa)$ values determined using different methods compared with the quantitative values obtained from the FT ($I_3/I_1 > I_{noise}$~0.01) analysis. The most common approach in DIW is to determine the end of the LVR when G_1' drops below 5% or 10% of G_1' within the LVR, which leads to smaller values for both ($\gamma_{NL}(\%)$ and $\sigma_y(Pa)$) compared to the FT analysis.

Formulations	$\gamma_{NL}(\%)$			
	$G_1' < 0.95G_{LVR}'$	$G_1' < 0.90G_{LVR}'$	Slope $\sigma\ (Pa)\ vs\ \gamma_0(\%)$ plot	$I_3/I_1 > I_{noise}$~0.01
F127	1.41	2.02	2.5	2.8
GO	0.13	0.19	0.6	0.9
	$\sigma_y(Pa)$			
	$G_1' < 0.95G_{LVR}'$	$G_1' < 0.90G_{LVR}'$	Slope in $\sigma\ (Pa)\ vs\ \gamma_0(\%)$ plot	$I_3/I_1 > I_{noise}$~0.01
F127	148	199	237	257
GO	11	17	43	52

Plotting LAOS data (from transient or correlation data collection) in different ways ($G_1'\ (Pa)$ and $G_1''\ (Pa)$ vs $\gamma_0\ (\%)$; and $\sigma(Pa)$ (stress amplitude) vs γ_0 (strain amplitude) plots) enable us to quantify the values of $\gamma_c(\%)$, $\sigma_y(Pa)$ and $\sigma_f(Pa)$. The stress-strain log-log plot helps identifying the "bulk flow" plateau and any potential issues such as the extreme behaviour observed for the GrGO formulation. This valuable and quantitative information might be easily dismissed if only the first harmonic moduli vs strain plot is provided.

D. Material measures of nonlinearities: G_M', $G_{L,}'$ S (dimensionless index of nonlinearity) and Chebyshev coefficients ($^{e_3}/_{e_1}$, $^{v_3}/_{v_1}$)

Using only the first harmonic moduli, it is not possible to quantify and compare the nonlinear behaviour of different formulations, nor to understand higher harmonics contributions to each of them. This section focuses on the analysis of material measures of nonlinearities for all the formulations in this work. This is to the best of our knowledge, the first time that an FT-analysis and quantification of material measures are applied to formulations for DIW. Our analysis focuses on the third harmonic contributions (the most relevant nonlinear contribution) to calculate $e_3,\ v_3, G_M', G_L',$ and S (eqs. in section II). First we quantitatively compare the behaviour of formulations prepared with F127 (figure 9); we then compare those prepared using GO as the only additive (figure 10); and at the end of the section we provide a comparison of all the formulations that contain graphite prepared either with F127, GO, or a mixture of both (figure 11).

***F127 formulations*.** F127 stock solution shows an extensive LVR region in the plots for all the material measures of nonlinearities ($G' = G_M' = G_{L,}'\ S = 0, e_3/e_1 = 0,\ v_3/v_1 \approx 0$, figure 9). It then shows an intense transition into the nonlinear regime, as γ_0 increases into the MAOS and LAOS ($\gamma_0 > \gamma_c$) regions; the slope on the plot S vs γ_0 is steep (indicated in figure 9b). This suggest that the network of F127 micelles undergoes intense changes in the LAOS region (see L-B plots in section E). The same trend is observed for the elastic Chebyshev coefficients (determined from the Fourier coefficients, eq. 2).[36] The elastic third harmonic Chebyshev coefficients (relative to the first harmonic) are negative ($^{e_3}/_{e_1} < 0$) for all F127 formulations in the nonlinear regime. The trends of the material measures, $e_3, G_M', G_L',$ and S for F127 indicate that the formulations undergo through intracycle strain softening.[36] Viscous Chebyshev coefficients, $^{v_3}/_{v_1}$ values (eq. 3) are ≈ 0 in the linear regime; become negative in the SAOS to MAOS transition; show a minimum value in the middle of the MAOS region; and then increase again eventually becoming positive further in the LAOS region (figure 9d). This indicates that the viscous component undergoes a transition from a shear thinning behaviour ($^{v_3}/_{v_1} < 0$),[36] to a shear thickening behaviour ($^{v_3}/_{v_1} > 0$)[36] as γ_0 increases. The addition of active materials (Gr and CNTs) to F127 stock solution has a considerable impact on nonlinear material measures: G_M', G_L' start to separate from G_1' at very small strain values, $\gamma_{NL}(\%) = 0.04$, as they enter into a MAOS region that spans across a wide range of strain values (figure 9). The linear regime (LVR) for these formulations (GrF127, and GrCNTsF127) is dramatically reduced compared to the linear regime for the F127 stock solution (figure 9). The active materials change the behaviour of the F127 hydrogel, which might no longer be a network of spherical micelles arranged in a cubic lattice.[46] This re-arrangement of F127 micelles when combined with different solid particles is yet to be studied. All the F127 formulations exhibit $G_M' > G_L'$ and $S < 0$ in the nonlinear regime, which corresponds to intra-cycle and inter-cycle strain softening.[35, 36] The nonlinear material measures values and trends for GrF127 and CNTsGrF127 formulations almost overlap (figure 9); it is clear that Gr powders have the biggest impact in the nonlinear behaviour. S and $^{e_3}/_{e_1}$ become negative at very small strains (figure 9b, c), with a very gradual as γ_0 increases through the extensive MAOS and LAOS regions. Linear and nonlinear parameters show that the GrF127 and GrCNTsF127 formulations undergo a more

gradual network breakdown into a broader nonlinear regime compared to the F127 formulation base. The viscous Chebyshev coefficients for GrF127 and GrCNTsF127 formulations show a peculiar trend (figure 9d); $^{v_3}/_{v_1}$ values gradually evolve from a plateau at slightly negative values ($^{v_3}/_{v_1} \sim -5\%$) to positive values in the MAOS region (figure 9d). The viscous component of these formulations undergoes a different transition than F127 due to the presence of solid particles; going from a slightly shear thinning behaviour to a shear thickening behaviour without showing a minimum value on the viscous Chebyshev coefficients (figure 9d). These results suggest that the addition of active materials has a different impact on the elastic and viscous contributions to the stress. In this case, the addition of powders to the F127 hydrogel changes the viscous component, while the elastic coefficients follow a similar trend for F127 formulations with and without added particles.

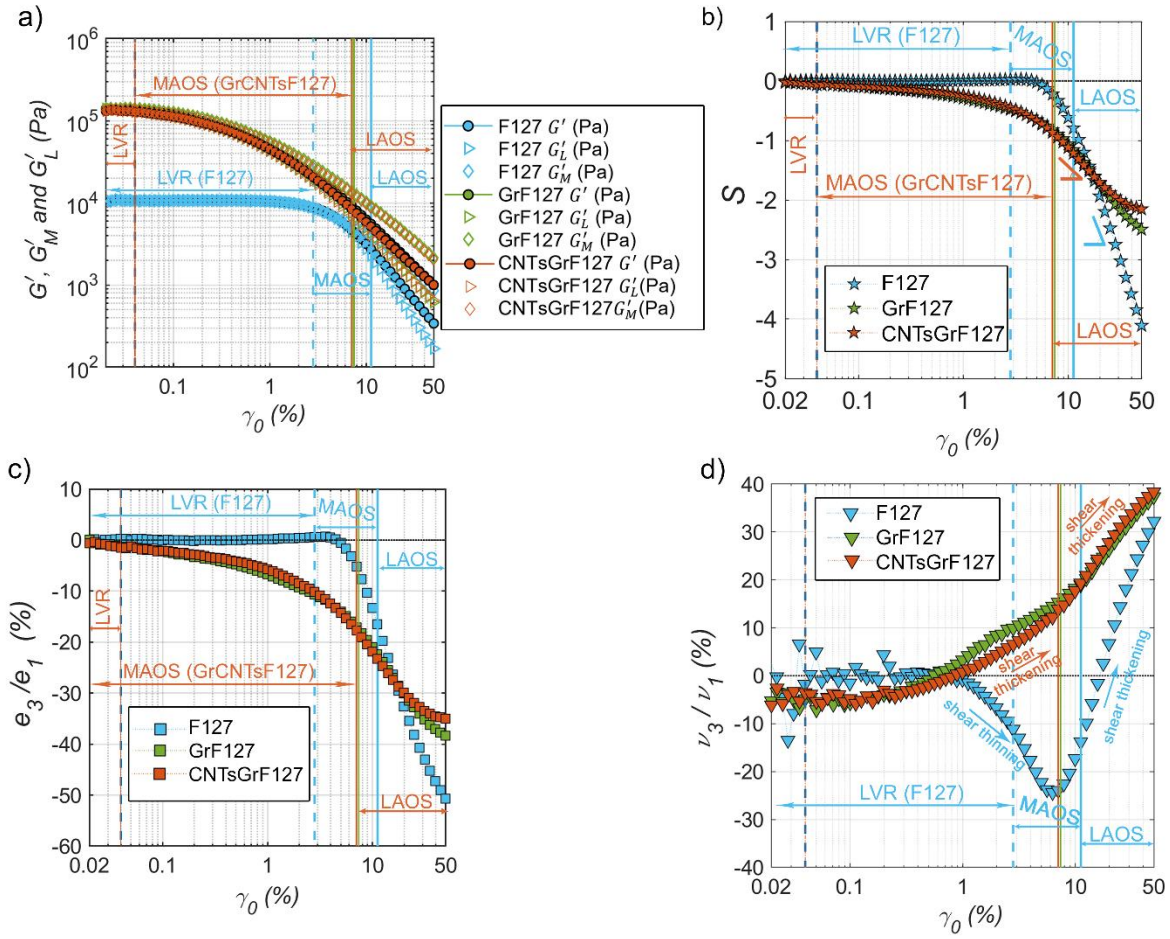

Figure 9. Material measures of nonlinearities for formulations prepared with F127 (F127 stock solution, GrF127, and GrCNTsF127): (a) Large (G'_L) and minimum (G'_M) strain moduli calculated from Chebyshev coefficients (equations 4, 5); (b) Dimensionless nonlinear coefficient (S) (eq. 6); (c) Elastic third harmonic Chebyshev coefficients relative to the first harmonic ($^{e_3}/_{e_1}$) (eq. 2); (d) Viscous third harmonic Chebyshev coefficients relative to the first harmonic ($^{v_3}/_{v_1}$) (eq. 3). Vertical dashed lines in the graphs represent the onset of nonlinearities ($\gamma_{NL}(\%)$) determined from the FT harmonic maps (figure 4, section III.B). Solid vertical lines in the graphs represent the critical strain values ($\gamma_c(\%)$) determined from the crossover of the first harmonic moduli (section III.C).

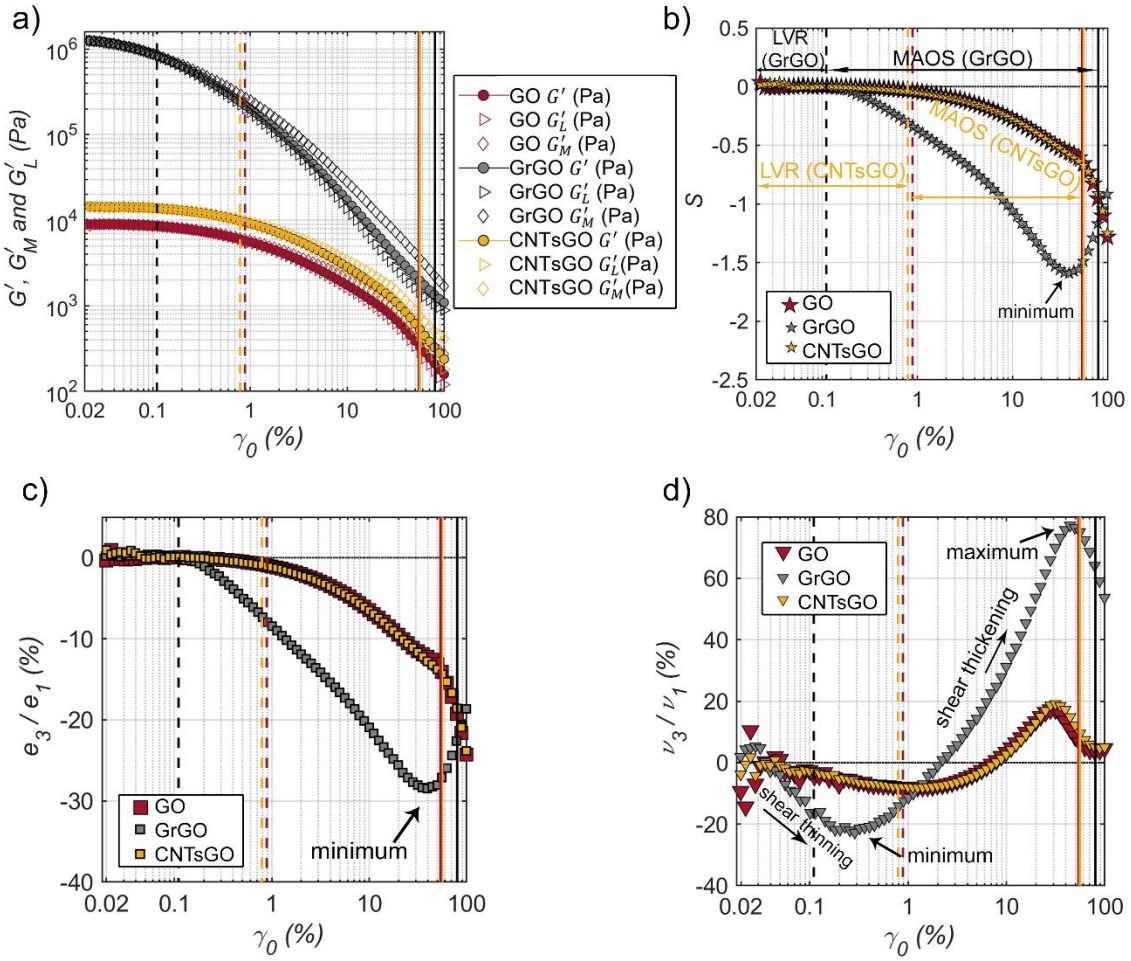

Figure 10. Material measures of nonlinearities for formulations prepared with GO (GO stock suspension, GrGO, and CNTsGO): (a) Large (G'_L) and minimum (G'_M) strain moduli calculated from Chebyshev coefficients (eqs. 4, 5); (b) Dimensionless nonlinear coefficient (S) (eq. 6); (c) Elastic third harmonic Chebyshev coefficients relative to the first harmonic ($^{e_3}/_{e_1}$) (eq. 2); (d) Viscous third harmonic Chebyshev coefficients relative to the first harmonic ($^{v_3}/_{v_1}$) (eq. 3). Vertical dashed lines in the graphs represent the onset of nonlinearities ($\gamma_{NL}(\%)$) determined from the FT harmonic maps (figure 4, section III.B). Solid vertical lines in the graphs represent the critical strain values ($\gamma_c(\%)$) determined from the crossover of the first harmonic moduli (section III.C).

GO formulations. The GO stock solution and CNTsGO formulation show almost identical values and trends for all the nonlinear material measures (figure 10). However, the not printable GrGO formulation shows clearly differentiated values and trends that are explained in detail in this section. For the printable GO formulations (GO and CNTsGO) the observed trends for nonlinear material measures, G'_M, G'_L, S, e_3, v_3, are very similar to those described for the F127 formulations containing active materials (discussed in the previous section). G'_M, G'_L separate from G'_1 in the MAOS region, with $G'_M > G'_L$ in the nonlinear regime (figure 10a). S and $^{e_3}/_{e_1}$ become negative at very small strains (figure 9b, c), with a very gradual as γ_0 increases through the extensive MAOS and LAOS regions. The not printable GrGO formulations has a narrow LVR, with G'_1, G'_M, and G'_L values ~2 orders of magnitude larger (same as for the linear, first harmonic moduli). We found that G'_1, G'_M, G'_L start to decrease even within the LVR quantified from the frequency analysis (figure 10a). The drop of G'_1, G'_M, and G'_L values within the LVR for GrGO (figure 10a), might be associated to viscous nonlinearities (figure 10d) but not elastic ones, given that $S \sim 0$ and $^{e_3}/_{e_1} \sim 0$ in the linear regime, while $^{v_3}/_{v_1} < 0$. The dimensionles index, S, becomes negative in the MAOS region (figure 10b) and

it reaches a minimum just before the MAOS to LAOS transition, as $\gamma_0 \to \gamma_c$. The elastic Chebyshev coefficient ($^{e_3}/_{e_1}$) follows exactly the same trend (figure 10c). The minimum values in both, S and ($^{e_3}/_{e_1}$), suggest that the GrGO formulation undergoes a transition from inter-cycle strain softening to stiffening. This shift has only been observed on this not-printable sample (figure 10, and L-B plots and analysis in the next section).

Viscous Chebyshev coefficients for all the GO formulations (printable and non-printable) show the following trend: $^{v_3}/_{v_1}$ values initially fluctuate due to noise at small strains. As γ_0 increases they stabilise and take very small negative values ($^{v_3}/_{v_1} < 0$, shear thinning) even within the LVR. $^{v_3}/_{v_1}$ values slightly decrease as γ_0 increases into MAOS, but a change of trend is observed within the MAOS region. The sign of the third harmonic viscous coefficients rapidly becomes positive ($^{v_3}/_{v_1} > 0$, shear thickening)[36], until they reach a maximum before decreasing again in the LAOS region (figure 10d). Although similar, the transition observed is more extreme for the not printable GrGO formulation with steeper slopes, with a $^{v_3}/_{v_1}$ minimum value of $\sim(-20\%)$ and a maximum value of $\sim(80\%)$ (figure 10d). For this sample, the maximum viscous Chebyshev third harmonic coefficient, and the minimum elastic Chebyshev third harmonic coefficient, take place at similar strain values $\gamma_0 \sim 40 - 45\%$, before reaching the critical strain $\gamma_0 = 80\%$ (table IV). These results demonstrate that the combination of different additives and active materials change the elastic and viscous contributions in different and unpredictable ways, that could only be revealed through the non-linear analysis. Therefore future studies will delve into strain decomposition and SPP approaches to improve our understanding of these yield stress fluids and soft solids.[13, 33, 53]

Comparison of Gr formulations. A comparison of the material measures of nonlinearities for all the formulations containing graphite powders in this work, including the hybrid formulation, is included in figure 11. The trends observed for the hybrid (S, e_3, and v_3 values) are very similar to all the other printable formulations that contain active materials apart from the not printable GrGO formulation. The hybrid and the GrF127 formulation have very similar linear and non-linear moduli values (figure 11a), while the not printable graphite formulation (GrGO) is clearly stiffer, with values for these moduli (G_1', G_M', and G_L') an order of magnitude higher.

The quantitative analysis of material measures of nonlinearities for DIW formulations shows that printable formulations with active materials behave in very similar ways, and that the impact of different ingredients (additives and active materials) on nonlinearities can be measured. For example, the printable F127 stock solution shows a 'clean' transition from linear to nonlinear behaviours, with an extensive LVR and a rapid breakdown of the microstructure. The other printable formulations in this work (F127 with active materials, GO and CNTsGO) show a very gradual transition into the nonlinear regime unlike F127 by itself. The non-printable GrGO formulation shows some distinctive features in the trends and magnitude of the viscous Chebyshev coefficients. Its behaviour shifts from shear thinning to shear thickening as the strain amplitude increases, which suggests that the viscous contributions have an important role in the (not printable) behaviour of this sample. Based on the results in this section, and with only one not printable formulation, we cannot yet establish a clear link between nonlinearities and printability. However, we can confidently say that the FT analysis and higher harmonics interpretation provide new insights to better understand yield stress fluids in DIW, and the role that different additives and active materials play in their rheology.

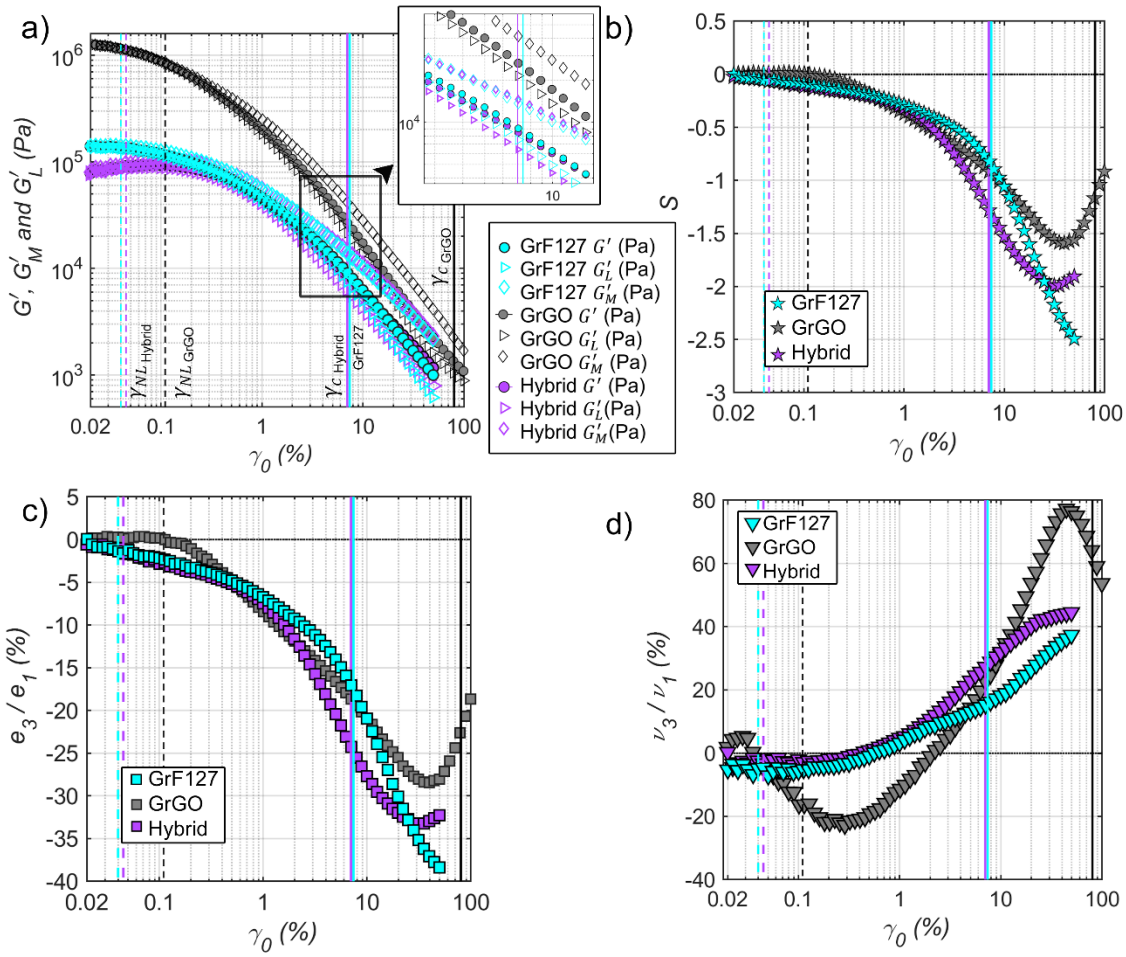

Figure 11. Material measures of nonlinearities for formulations that contain Gr particles (GrF127, GrGO and hybrid): (a) Large (G'_L) and minimum (G'_M) strain moduli calculated from Chebyshev coefficients (eqs. 4, 5); (b) Dimensionless nonlinear coefficient (S) (eq. 6); (c) Elastic third harmonic Chebyshev coefficients relative to the first harmonic ($^{e_3}/_{e_1}$) (eq. 2); (d) Viscous third harmonic Chebyshev coefficients relative to the first harmonic ($^{v_3}/_{v_1}$) (eq. 3). Vertical dashed lines in the graphs represent the onset of nonlinearities ($\gamma_{NL}(\%)$) determined from the FT harmonic maps (figure 4, section III.B). Solid vertical lines in the graphs represent the critical strain values ($\gamma_c(\%)$) determined from the crossover of the first harmonic moduli (section III.C).

E. Lissajous analysis

3D Lissajous spaces ($\sigma(t)$, $\gamma(t)$, $\dot{\gamma}(t)$) elastic, viscous, and normalised elastic L-B curves for all the formulations including all the waves are provided in the supporting information (figures S6-S8). Here we include selected L-B curves in the SAOS, MAOS and LAOS (F127 and GO formulations in figures 13 and 15 respectively) that show differences and similarities between the formulations.

F127 formulations. In the *SAOS region* (figure 12a) the F127 stock solution shows a predominantly elastic response in the LVR up to the onset of nonlinearities ($\gamma_{NL} = 2.8$ %, table IV). The widening of elliptical curves in the elastic Lissajous plots evidence that the addition of active materials (Gr and CNTs) to F127 leads to a viscoelastic behaviour in the LVR with an increased viscous contribution (figure 12b, c). The ellipse is even wider for the hybrid formulation (figure 12d). In the *MAOS region,* the nonlinearities emerge as strain increases and non-elliptical distortions appear in the L-B plot. The large and minimum storage moduli G'_M, and G'_L can, in principle, be determined directly from the L-B plots (figure 12a, MAOS).

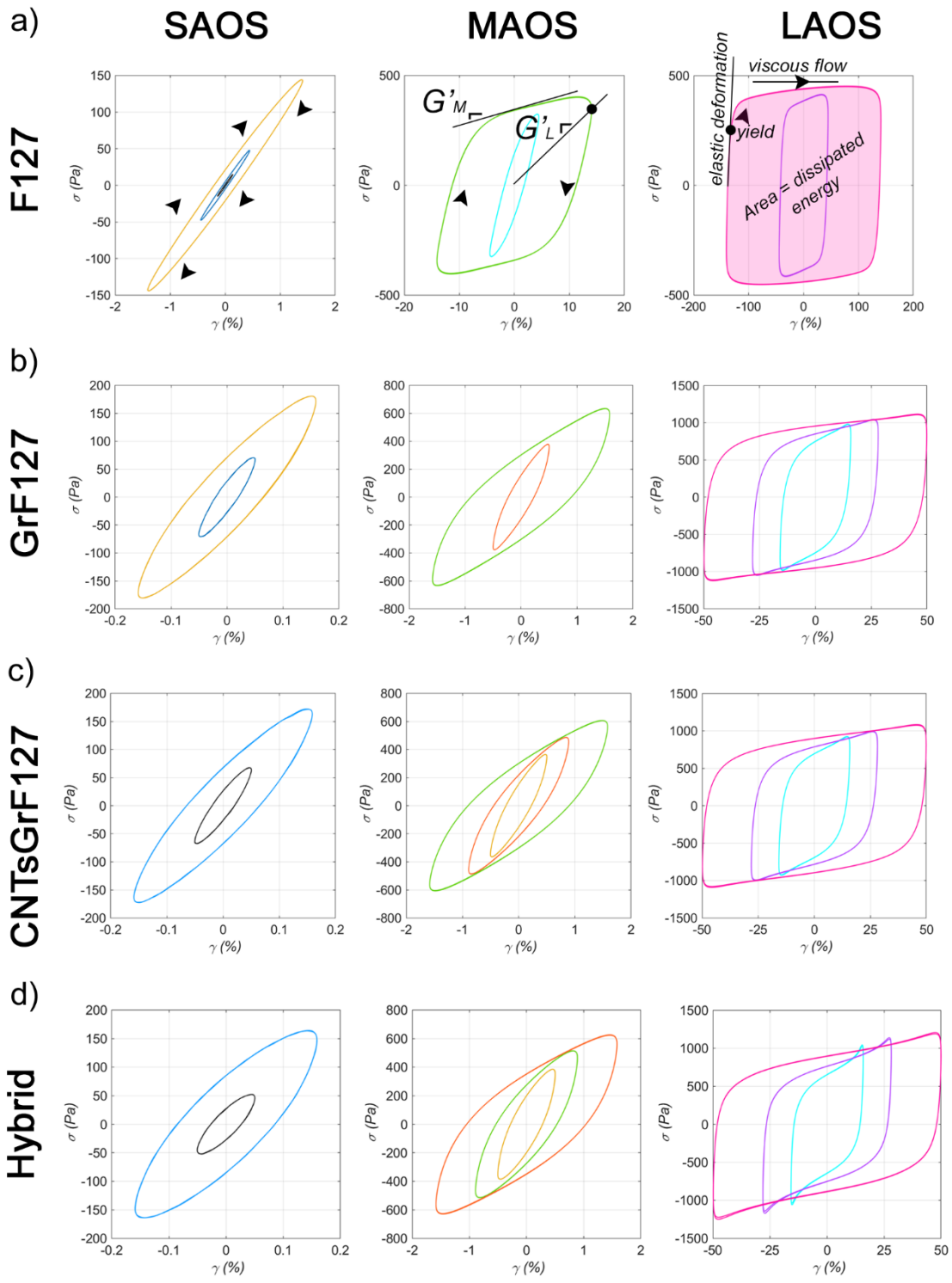

Figure 12. Elastic Lissajous-Bowditch plots in the SAOS, MAOS and LAOS regions for F127 formulations with and without active materials: (a) F127, (b) GrF127, (c) CNTsGrF127, and d) Hybrid formulation. The arrows (in a) indicate the direction of the wave for all the LAOS tests. A visual representation of how to determine the local nonlinear elastic moduli: G'_M, and G'_L is included in (a, MAOS). The highlighted area (a, LAOS) illustrates the energy dissipated within a LAOS cycle.

From a careful look on the L-B shapes, it strikes that $G'_L > G'_M$ for all the formulations in the MAOS region, which contradicts our Chebyshev analysis (in section D). To confirm this observation, the elastic nonlinear moduli for the F127 stock solution have been calculated and compared using the two methods: 1) from the Chebyshev analysis including higher harmonics

up to n = 11, and 2) from the local slopes in the L-B curves at zero strain (tangent modulus, G'_M), and at maximum strain (secant modulus, G'_L). The results of this analysis confirm the discrepancy (figure 13). The values calculated using the two methods match within the LVR, however they divert in the nonlinear regime, thus confirming that $G'_L > G'_M$ based on the L-B plots, which is associated with strain stiffening behaviour within a LAOS cycle.[36] While the Chebyshev analysis including harmonics up to *n* =11, confirms that e_3 takes negative values (figure 13a) and that $G'_L < G'_M$ for all the strains in the sweep (figure 13c, d) which are associated with strain softening. This rather confusing contradiction or 'paradox' has been previously discussed in literature, and that this can be explained by the sensitivity of local measures of elasticity to the rate of the deformations, which is not constant within a LAOS cycle.[38, 57] The fact is that all the formulations are clearly strain softening as the strain amplitude increases in the sweep, and that G'_1, G'_M, and G'_L all considerably decrease in LAOS, up to ~3 or more orders of magnitude.

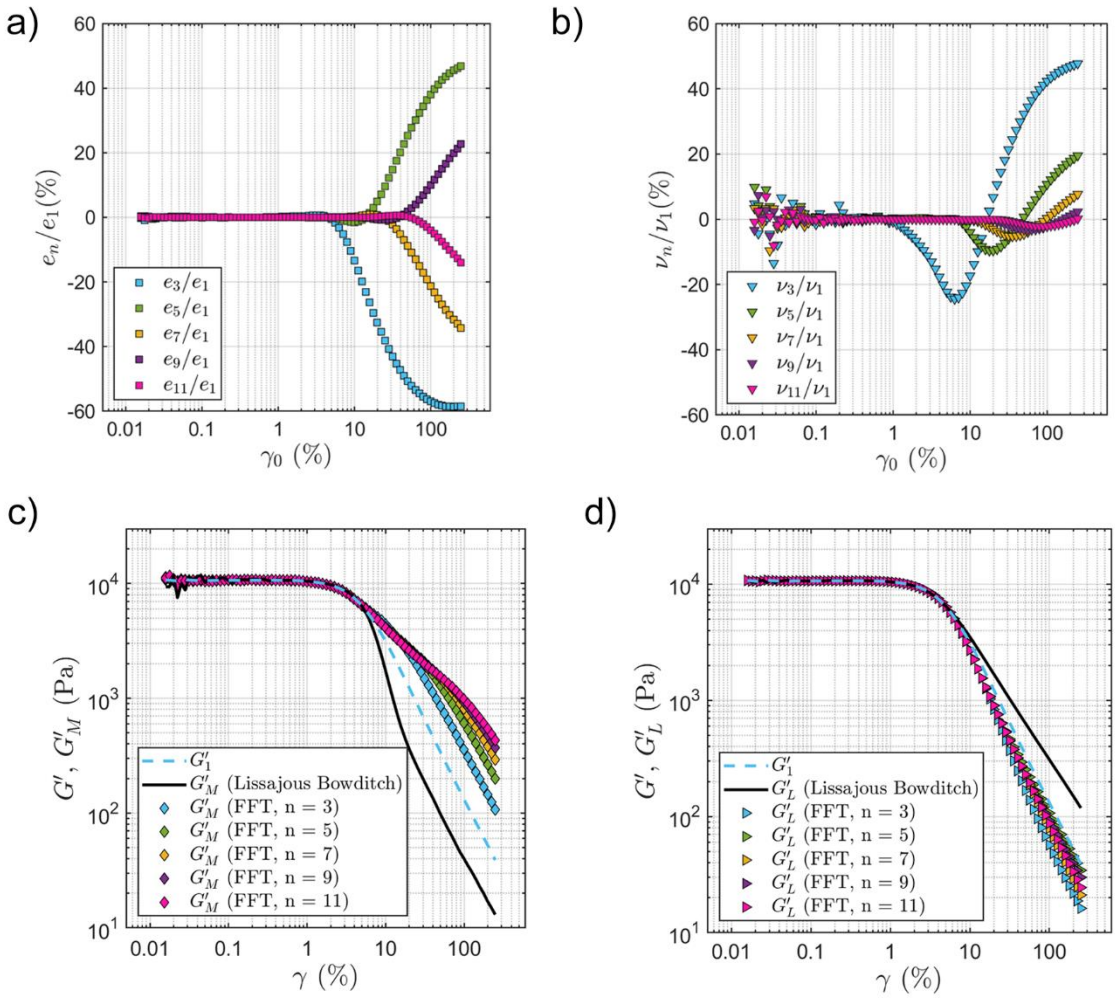

Figure 13. Chebyshev coefficients of higher order (up to n=11) for F127 formulation base: (a) Elastic, e_n, and b) Viscous, v_n, (obtained using equations 2, and 3). Comparison of G'_1, G'_M (in c) and G'_L (in d) values obtained from the Chebyshev coefficients (symbols) vs the values obtained directly from the elastic Lissajous-Bowditch (black line) plots included in figures 13(a, b) and 12, respectively.

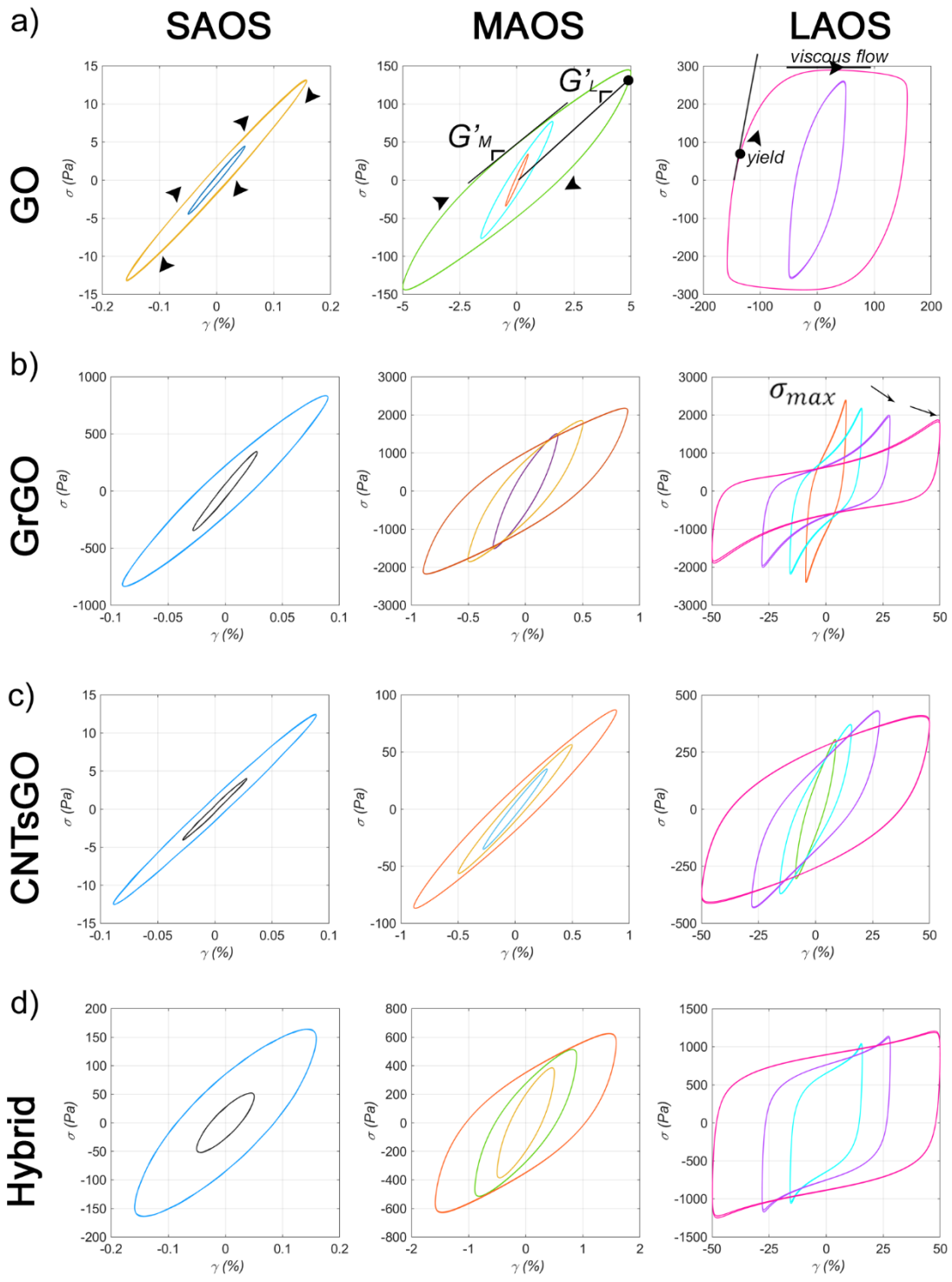

Figure 14. Elastic Lissajous-Bowditch plots in the SAOS, MAOS and LAOS regions for formulations with and without active materials: (a) GO stock suspension, (b) GrGO, (c) CNTsGrGO, and d) Hybrid formulation. The arrows (in a) indicate the direction of the wave for all the LAOS tests. A visual representation of how to determine the local nonlinear elastic moduli: G'_M, and G'_L is included in (a, MAOS). The highlighted area (a, LAOS) illustrates the energy dissipated within a LAOS cycle.

LAOS region. The L-B curves for F127 (figure 12a, LAOS) get close to a perfect square (when axes are normalised, figure S7 in the supporting information) in the nonlinear regime. Square shapes in elastic Lissajous curves are associated with plasticity,[38] a perfect plastic response would correspond to the maximum possible dissipated energy for a given strain amplitude γ_0

and maximum stress σ_{max}. In the L-B curve for F127 at the largest strain amplitude in the sweep (figure 12a, LAOS) we can also point out the yield point that shows the transition from purely elastic behaviour, to yield into viscoelastic and viscous flow at the top of the curve (plateau at the maximum stress σ_{max}). The perfect plastic dissipation ratio (ϕ) defined in section II (eq. 7), is said to be a well-defined material measure with almost no sensitivity to the data acquisition rate (or rate of deformations).[38] Here we use this metric to compare the formulations in this work and to quantify how close or far they are from the perfect plastic behaviour. F127 shows an almost purely elastic behaviour in SAOS ($\phi \sim 0$, figure 15) and gets close to an ideal plastic behaviour in LAOS as $\phi \to 1$. Xanthan gum and drilling fluids are examples of yield stress fluids that exhibit some similarities with the F127 stock solution.[38] However when active materials are added (figure 12b and c), the curves in the LAOS region change shape, the transition between elastic deformation and viscoelastic flow is not easy to distinguish within a LAOS cycle, because the L-B shape becomes smoother with softer edges in the LAOS region (figure 12bd, LAOS). The dissipation ratio trends for F127 formulations confirm that the addition of active materials increases the viscous contributions in the SAOS region ($\phi \sim 0.3$, figure 15a). The dissipation ration in LAOS for GrF127, CNTsGrF127 and hybrid formulations show values in the range between $\phi \sim 0.7$ and 0.8 (figure 15a), which is associated with Newtonian behaviour instead of ideal plastic. These results suggest that the pure F127 stock solution can be classified as an elastoplastic material, while "filled" F127 formulations with carbon materials are viscoelastic.

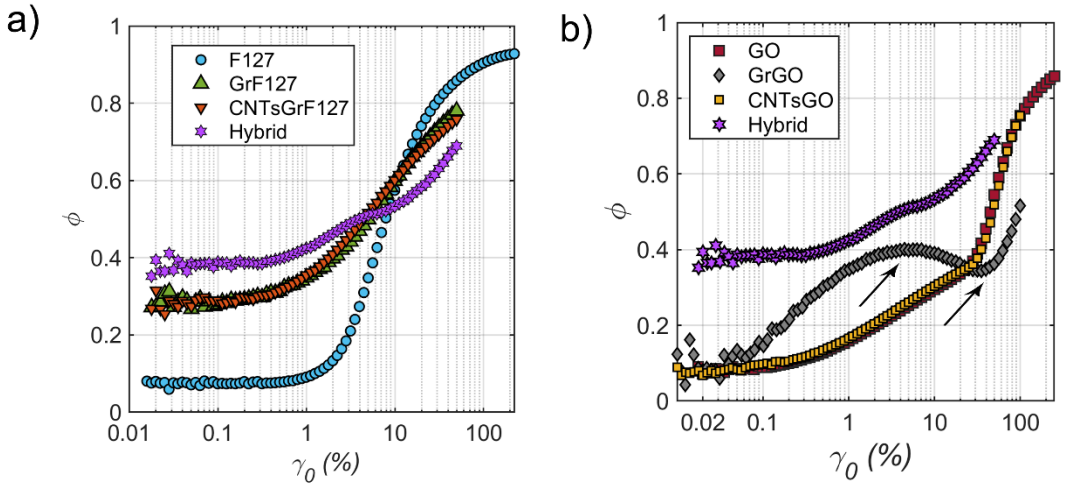

Figure 15. Evolution of the perfect plastic dissipation ratio, ϕ (calculated using eq. 7) for: (a) F127 formulations and (b) GO formulations. The results for the hybrid formulations are included in both graphs for comparative purposes. F127 stock solution is the closest formulation to a perfect plastic behaviour in LAOS. For the not printable formulation (GrGO, black diamonds in b) ϕ values go through different trends (with a maximum and a minimum) within the MAOS region during the yielding of the sample.

GO formulations. The L-B plots for the printable GO formulations (figure 14a, c) show similar shapes and trends than the "filled" F127 formulations with active materials (for all three SAOS, MAOS and LAOS regimes), but the L-B plots for the non-printable formulation, GrGO (figure 14b), has very distinctive shapes in the LAOS region.

In the *SAOS region* GO stock solution and CNTsGO formulation shows a predominantly elastic behaviour based on both the L-B plots (figure 14a, c) and the values of dissipation ratio ($\phi < 0.1$, figure 15b). The L-B plots show elliptical distortions at very small strain values for the non-printable GrGO formulation (figure 14b). In the *MAOS* and *LAOS regions*, the differences between printable and non-printable GO formulations become evident. The GrGO formulation shows extreme distortions (figure 14b), with upturns at the maximum strain within

a LAOS cycle. It is also possible to identify the peak of the stress amplitude (σ_{max}), which has been discussed in detail in section C. The values of the dissipation ratio, ϕ, for this formulation show a non-monotonic trend unlike the printable formulations (figure 15b). In SAOS, ϕ varies arbitrarily between 0 and 0.2; it then increases in MAOS reaching a first maximum value $\phi \sim 0.4$ at 5% strain amplitude (γ_0); it then goes through a minimum and increases again up to $\phi \sim 0.5$ at γ_0=100%.

The visual representations of LAOS results in L-B curves provide a very useful tool to identify nonlinear behaviours of printable (or not) formulations. These plots can be easily generated from a standard LAOS test without needing to delve into a quantitative nonlinear analysis. DIW users can benefit from monitoring and reporting these curves, to help with the analysis and discussion of the yielding transition, and to compare formulations with different compositions. Even in the absence of frequency analysis or quantitative measures of higher harmonics contributions, Lissajous plots will help researchers to better understand their formulations and identify potential issues in their microstructure and printability. The determination of the dissipation ratio combined with the Lissajous analysis complements the findings from the frequency analysis (section III.B), the stress-strain plots (section III.C) and the quantitative materials measures of nonlinearities (section III.D). This 'well-behaved' scalar measure[38] with almost no sensitivity to the acquisition rate seems capable of differentiating printable and non-printable formulations. Although a clear link between the dissipation ratio and 'printability' cannot be drawn quite yet given the reduced number of formulations studied here, ϕ is a promising metric to characterise the behaviour of DIW formulations.

F. 'Printability' maps using Ashby-type material measures charts

In the previous sections we provide the quantitative analysis and qualitative visual representations of LAOS results for a library of soft solids designed for 3D printing of conductive 3D architectures. We have described the concept of 'printability' and the printability of our formulations in the introduction and in section A, although an automatised system to objectively judge 'print quality' has not been used, and therefore this judgment might be subjective. However, in this relatively broad definition we also must account for the wide range of applications involved, and that 'printability' requirements and maps, need to be tuned accordingly. This determines the level of control and accuracy to realise complex features in 3D shapes. Bioprinting applications might require moderate G', and low σ_f values to guarantee cell survival and proliferation,[8-10] while other applications might require an accurate control of fine features, such as unsupported overhangs, which need higher G', and σ_f values. The map here discussed focuses on formulations of carbon-based and other 2D materials for energy applications. We have previously described the printability of soft materials based on the following bulk rheological parameters: $G', \sigma_f,$ and FTI.[27] The storage modulus (G') and the yield (or flow) stress (σ_y^*) are frequently used to describe 'printability'.[31, 34, 62, 63] However, note the asterisk to flag the lack of consistency within the DIW field on the yield (or flow) stress determination. For example, σ_y^* could be determined from fitting continuous shear (flow ramps) data; from the stress determination at the end of the LVR; or the stress at the solid-to-liquid transition ($G' = G''$). This leads to inconsistencies and lack of consensus when discussing printability. Similarly to Ashby's materials selection charts,[39] we can create maps that compile linear material measures G', vs σ_y^* on the coordinate axes for different formulations, that can be obtained from a standard LAOS test without the need of doing an FT analysis. We provide here Ashby-type 'printability' maps using the results from this work (figure 16a) and for context, we populate this map with data from other formulations found in published literature (figure 16b). A clear correlation between nonlinearities and 'printability' cannot be concluded from the

FT analysis performed on a relatively small set of samples (only just one of them being not printable). What we can confidently conclude from our analysis though, is that the trends of nonlinear parameters for all the printable formulations are the same. Our long-term aim is to expand our analysis to a larger set of samples in DIW for different applications and expand these 'printability' maps to include linear and nonlinear material measures, and scalar metrics such as the dissipation ratio. We will also delve into additional tools, such as the Sequence of Physical Processes (SSP) developed by Rogers et al.,[50-52] however this is currently beyond the scope of this manuscript.

The 'printability' map, based on linear material measures, for the formulations studied in this work shows that all the printable formulations are contained within a small region (highlighted in turquoise, figure 16a), while the non-printable GrGO formulation is far from it, due to its high stiffness and the stress peak on the stress-strain curve (section C). The map also includes dashed lines delimiting the region of interest in which our formulations fall: two vertical lines for flow stress limits ($\sigma_f = 500\ Pa$ and $\sigma_f = 1500\ Pa$) chosen based on our empirical evidence, and a diagonal line that represents the figure of merit ($FoM = {G'}/{\sigma_f} = 20$).[62] The printability region is not "rigid", its boundaries can be blurred: softer formulations ($G' \downarrow,\ \sigma_f \downarrow$) located towards the left on the map and close to the diagonal (area highlighted in light colour) might be suitable for 3D printing of parts with limited complexity. As we move towards the right and upwards from the dashed diagonal on the map, we find stiffer formulations ($G' \uparrow,\ \sigma_f \uparrow$, area highlighted in darker colour) that provide better print quality.

For example, the F127 stock solution can be 3D printed to make relatively simple parts with vertical walls (images in figure 16a), while the hybrid formulation can also be used to build complex parts with fine features (images in Figure 16a). It must also be considered that the density and concentration of the materials in the formulation, and whether the printing takes place in air, inside another gel, or an oil bath, will affect the required $G',\ \sigma_f$ values for that formulation to be printable.[64] We find some limitations to build reliable maps in context with data from literature, because the quality of the data collected is often uncertain, or the analysis is not explicit (figure 16b). Despite the barriers, we find that most of the formulations labelled as 'printable' in the literature here included, fall within the printable regions discussed above. These maps can be a very useful tool in formulation design if they were carefully populated with reliable data. However, we affirm that they should not be used in isolation, because this could lead to an oversimplification of the analysis and overlooking signs of unusual behaviours.

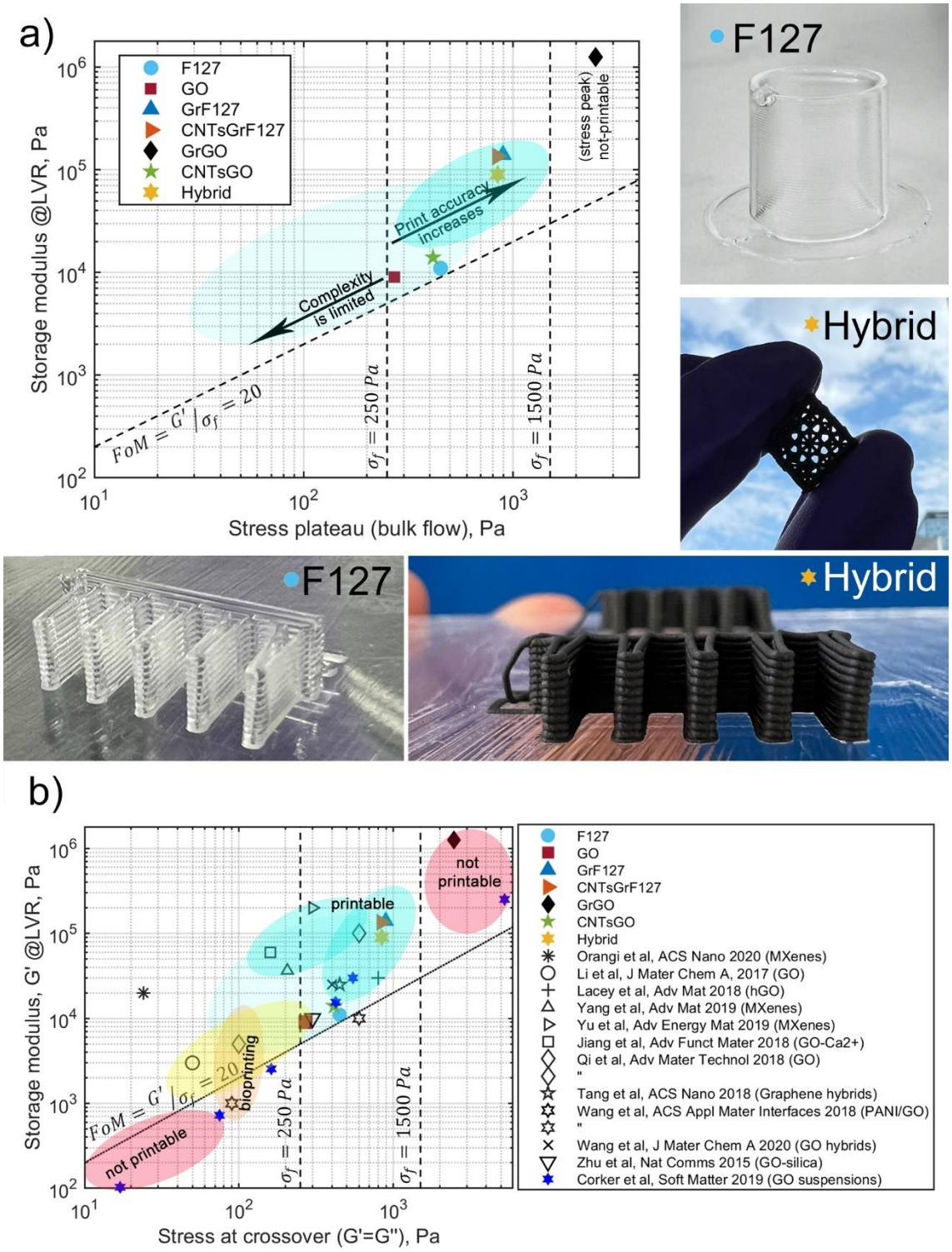

Figure 16. Defining 'printability' using Ashby-type[39] charts of material measures (G', vs σ_y^*) focused on formulations for energy applications: a) Map for the formulations studied in this work, accompanied by images exemplifying print quality for F127 stock solution (●), and Hybrid formulation (★). b) Map comparing the formulations in this work, with our previous defined printability window for GO suspensions,[27] and data from published literature on 3D architectures made of 2D materials for energy applications.[1, 2, 20, 23, 28, 65-70] Printable and not printable formulations are highlighted in turquoise and red respectively. The yellow area illustrates an 'in-between' transition region, in which the complexity of printed parts is limited. The region in orange highlights the area in which some bioprinting applications would fall, with stress values σ_f~100 Pa. *Note that the data taken from literature had to be read from graphs, as they were not explicitly discussed in most cases. For consistency, we have chosen the stress values at the cross-over point from LAOS data (stress vs strain data were not provided in any of these publications).

CONCLUSIONS

The rheology of yield stress fluids and studies of their LAOS behaviours are active and long-standing research fields, while DIW, or 3D printing of soft matter is an emerging research area that is quickly expanding. Here we aimed to build a bridge between more specialised rheology studies on yield stress fluids, with the growing diverse community exploiting DIW in different applications. This work provides to the multidisciplinary community in DIW, guidance to improve data collection, and tools to perform deeper analysis of LAOS tests (including visual and qualitative analysis of Lissajous-Bowditch curves; yielding transition quantification in stress-strain curves; frequency analysis and quantification of higher harmonics, as well as material measures of nonlinearities). This work has focused on LAOS of soft solids designed for 3D printing carbon-based conductive structures. Our library is a small but fair representation of the different materials and formulation approaches currently being developed, and unintentionally has provided us with an opportunity to compare printable and non-printable formulations. From the results organised in different sections, we can draw the following conclusions summarising our findings.

FT rheology of raw data signals enables us to quantify nonlinearities and to create 3D maps to visualise the onset and rising of higher harmonics contributions. We have shown how 2D projections of these maps can be used to carry out quantitative comparisons of different formulations and to identify the role that different additives and active materials play in the yielding transition. Quantitative material measures of nonlinearities (Fourier coefficients (G_1', G_1'', G_3', G_3'', etc.); Chebyshev coefficients (e_1, v_1, e_3, e_3 etc.); elastic moduli (G_M', G_L'); and dimensionless index of nonlinearity (S) have enabled us to explore the higher harmonics contributions and how they change for different additives and active materials. Although all the formulations in this work have shown broadly similar trends (most of them showed type I behaviour), each of them has characteristic values for material measures in the linear and nonlinear regime. We have objectively determined: the onset of nonlinear behaviours (end of LVR, γ_{NL}) from harmonics maps; and the yielding transition and bulk flow stress (σ_f) from stress-strain graphs. Finding the limits of the LVR for DIW formulations can be extremely subjective, its end is sometimes delimited considering a drop to ~90% of the at rest storage modulus, G'_{LVR}. The FT analysis enables to precisely quantify the onset of nonlinear behaviours and to evaluate how this is affected by the addition of different active materials and additives. This analysis will be very useful to those working in bespoke additives and formulation design, for example in the synthesis of new generations of responsive surfactants.

We have encountered contradicting results between the Chebyshev analysis and the determination of G_M', G_L' from local slopes in the L-B curves that can be explained due to the sensitivity of local measures of elasticity to the data acquisition rate. An alternative scalar metric, the dissipation ratio, ϕ (which is less sensitive to the rate of deformations) is a promising parameter to characterise the behaviour of complex fluids designed for DIW.

The stress-strain log-log plots and the Lissajous-Bowditch curves displayed singular features for the non-printable formulation (GrGO) that clearly differentiate it from printable ones. This formulation reached an extremely high stress peak or maximum within the yielding transition instead of the plateau associated with bulk flow that printable formulations displayed. This undesired behaviour is clearly seen in the stress-strain plot, in the non-monotonic trend of the perfect plastic dissipation ratio, ϕ, and the L-B plots in the LAOS region. Our analysis and results flagged issues that would have been overlooked if the analysis was based only on the first harmonic moduli (G', G'' vs γ_0) plot. The viscous Chebyshev coefficients have also shown an extreme behaviour for the non-printable formulation. We have demonstrated the value of performing a deeper analysis of the raw data signals, quantitatively (through frequency analysis and quantifying material measures of higher harmonics contributions) and

qualitatively (through Lissajous analysis) to achieve a deeper understanding of printable and non-printable formulations.

Ashby-type charts based on linear material measures, G' vs σ_f on the coordinate axes, are very useful 'printability' maps to guide formulation design and pave the wave for common protocols and standards in DIW. In this map, focused on formulations for energy applications, we have delimited our printable region using the results from this work. We have expanded its boundaries using data from literature and discussed the needs of different applications. Printable formulations can range from 'soft' for the printing of simpler 3D shapes with limited complexity (for example in bioprinting applications) to 'stiff' for the accurate printing of complex shapes with fine features. We would like to emphasise the importance of using these maps alongside other quantitative measures (stress-strain log-log plots) and/or visual representations (Lissajous analysis) of LAOS results to avoid overlooking the signs that we have associated with poor printing performance. Although the link between nonlinear materials measures and 'printability' does not clearly emerge yet from the analysis of a small set of formulations, we have demonstrated that the combination of quantitative material measures, visual Lissajous-Bowditch representations and Ashby-type charts are a powerful approach to fully characterise complex fluids in 3D printing, and to guide the design of new additives and formulations.

SUPLEMENTARY MATERIAL

See supplementary material for additional information in data collection, additional figures, and discussion to support sections III.B (stress waves and FT 3D maps for all the samples are provided) and III.E (including 3D Lissajous spaces, elastic and viscous projections with all the waves for each of the formulations).

ACKNOWLEDGEMENTS

This work was supported by a UKRI Future Leaders Fellowship MR/V021117/1.

AUTHOR CONTRIBUTIONS (CRediT)

EGT led the work, carried out and supervised data collection, performed the analysis, and wrote the manuscript. RA assisted with the analysis during the revision stage and helped with the editing of the final manuscript. BL characterised the raw materials, prepared the formulations and carried out some of the data collection. DJCD assisted with the analysis, data processing and helped with the editing of the final manuscript.

No conflicts of interest

The authors have no conflicts to disclose.

REFERENCES

1. W. Yang, J. Yang, J. J. Byun, F. P. Moissinac, J. Xu, S. J. Haigh, M. Domingos, M. A. Bissett, R. A. Dryfe and S. Barg, Advanced Materials **31** (37), 1902725 (2019).
2. L. Yu, Z. Fan, Y. Shao, Z. Tian, J. Sun and Z. Liu, Advanced Energy Materials **9** (34), 1901839 (2019).
3. E. García-Tuñon, S. Barg, J. Franco, R. Bell, S. Eslava, E. D'Elia, R. C. Maher, F. Guitian and E. Saiz, Advanced materials **27** (10), 1688-1693 (2015).
4. V. G. Rocha, E. García-Tuñón, C. Botas, F. Markoulidis, E. Feilden, E. D'Elia, N. Ni, M. Shaffer and E. Saiz, ACS applied materials & interfaces **9** (42), 37136-37145 (2017).
5. E. Feilden, C. Ferraro, Q. Zhang, E. García-Tuñón, E. D'Elia, F. Giuliani, L. Vandeperre and E. Saiz, Scientific reports **7** (1), 1-9 (2017).

6. B. G. Compton and J. A. Lewis, Advanced materials **26** (34), 5930-5935 (2014).
7. M. E. Cooke and D. H. Rosenzweig, APL bioengineering **5** (1), 011502 (2021).
8. I. S. Kinstlinger and J. S. Miller, Lab on a Chip **16** (11), 2025-2043 (2016).
9. J. Lai, C. Wang and M. Wang, Applied Physics Reviews **8** (2), 021322 (2021).
10. M. Müller, J. Becher, M. Schnabelrauch and M. Zenobi-Wong, Biofabrication **7** (3), 035006 (2015).
11. R. H. Ewoldt, M. T. Johnston and L. M. Caretta, in *Complex fluids in biological systems* (Springer, 2015), pp. 207-241.
12. A. Ettehadi, C. Ülker and G. Altun, Journal of Petroleum Science and Engineering **208**, 109536 (2022).
13. J. J. Griebler and S. A. Rogers, Physics of Fluids **34** (2), 023107 (2022).
14. C. Saengow, A. J. Giacomin and A. S. Dimitrov, Physics of Fluids **31** (11), 111903 (2019).
15. Y. Wei, R. Li and H. Zhang, Physics of Fluids (2022).
16. D. De Kee, Physics of Fluids **33** (11), 111301 (2021).
17. S. Lee, S. R. Kim, H.-J. Lee, B. S. Kim, H. Oh, J. B. Lee, K. Park, Y. J. Yi, C. H. Park and J. D. Park, Physics of Fluids **34** (10), 103109 (2022).
18. E. Feilden, E. García-Tuñón, F. Giuliani, E. Saiz and L. Vandeperre, Journal of the European Ceramic Society **36** (10), 2525-2533 (2016).
19. J. A. Lewis, J. E. Smay, J. Stuecker and J. Cesarano, Journal of the American Ceramic Society **89** (12), 3599-3609 (2006).
20. C. Zhu, T. Y.-J. Han, E. B. Duoss, A. M. Golobic, J. D. Kuntz, C. M. Spadaccini and M. A. Worsley, Nature communications **6** (1), 1-8 (2015).
21. B. Shriky, A. Kelly, M. Isreb, M. Babenko, N. Mahmoudi, S. Rogers, O. Shebanova, T. Snow and T. Gough, Journal of colloid and interface science **565**, 119-130 (2020).
22. E. García-Tuñón, E. Feilden, H. Zheng, E. D'Elia, A. Leong and E. Saiz, ACS applied materials & interfaces **9** (38), 32977-32989 (2017).
23. Y. Jiang, Z. Xu, T. Huang, Y. Liu, F. Guo, J. Xi, W. Gao and C. Gao, Advanced Functional Materials **28** (16), 1707024 (2018).
24. L. R. d. C. Moraes, H. Ribeiro, E. Cargnin, R. J. E. Andrade and M. F. Naccache, Journal of Non-Newtonian Fluid Mechanics **286**, 104426 (2020).
25. S. Naficy, R. Jalili, S. H. Aboutalebi, R. A. Gorkin III, K. Konstantinov, P. C. Innis, G. M. Spinks, P. Poulin and G. G. Wallace, Materials Horizons **1** (3), 326-331 (2014).
26. C. Zhu, T. Han, E. B. Duoss, A. M. Golobic, J. D. Kuntz, C. M. Spadaccini and M. A. Worsley, Nature communications **6** (1), 1-8 (2015).
27. A. Corker, H. C.-H. Ng, R. J. Poole and E. García-Tuñón, Soft Matter **15** (6), 1444-1456 (2019).
28. S. D. Lacey, D. J. Kirsch, Y. Li, J. T. Morgenstern, B. C. Zarket, Y. Yao, J. Dai, L. Q. Garcia, B. Liu and T. Gao, Advanced Materials **30** (12), 1705651 (2018).
29. C. Zhu and J. E. Smay, Journal of Rheology **55** (3), 655-672 (2011).
30. A. M'barki, L. Bocquet and A. Stevenson, Scientific reports **7** (1), 1-10 (2017).
31. L. del-Mazo-Barbara and M.-P. Ginebra, Journal of the European Ceramic Society **41** (16), 18-33 (2021).
32. J. D. A Jeffrey Giacomin, in *Techniques in Rheological Measurement* (Chapman and Hall, 1993), pp. 99-121.
33. K. Kamani, G. J. Donley and S. A. Rogers, Physical review letters **126** (21), 218002 (2021).
34. A. Corker, University of Liverpool, 2022.
35. K. Hyun, M. Wilhelm, C. O. Klein, K. S. Cho, J. G. Nam, K. H. Ahn, S. J. Lee, R. H. Ewoldt and G. H. McKinley, Progress in Polymer Science **36** (12), 1697-1753 (2011).
36. R. H. Ewoldt, A. Hosoi and G. H. McKinley, Journal of Rheology **52** (6), 1427-1458 (2008).
37. D. Coblas, D. Broboana and C. Balan, Polymer **104**, 215-226 (2016).
38. R. H. Ewoldt, P. Winter, J. Maxey and G. H. McKinley, Rheologica acta **49** (2), 191-212 (2010).
39. M. F. Ashby and D. Cebon, Le Journal de Physique IV **3** (C7), C7-1-C7-9 (1993).

40. K. Hyun, J. G. Nam, M. Wilhellm, K. H. Ahn and S. J. Lee, Rheologica acta **45** (3), 239-249 (2006).
41. L. Du, M. Namvari and F. J. Stadler, Rheologica Acta **57** (5), 429-443 (2018).
42. J. Ma, P. Wang, L. Dong, Y. Ruan and H. Lu, Journal of colloid and interface science **534**, 12-19 (2019).
43. J. Franco, P. Hunger, M. E. Launey, A. P. Tomsia and E. Saiz, Acta biomaterialia **6** (1), 218-228 (2010).
44. M. Jalaal, G. Cottrell, N. Balmforth and B. Stoeber, Journal of Rheology **61** (1), 139-146 (2017).
45. C. C. Hopkins and J. R. de Bruyn, Journal of Rheology **63** (1), 191-201 (2019).
46. R. Ivanova, B. Lindman and P. Alexandridis, Langmuir **16** (23), 9058-9069 (2000).
47. R. Linemann, J. Läuger, G. Schmidt, K. Kratzat and W. Richtering, Rheologica acta **34** (5), 440-449 (1995).
48. J. Kim, L. J. Cote and J. Huang, Accounts of chemical research **45** (8), 1356-1364 (2012).
49. K. S. Cho, K. Hyun, K. H. Ahn and S. J. Lee, Journal of rheology **49** (3), 747-758 (2005).
50. S. A. Rogers and M. P. Lettinga, Journal of rheology **56** (1), 1-25 (2012).
51. S. A. Rogers, B. M. Erwin, D. Vlassopoulos and M. Cloitre, Journal of Rheology **55** (2), 435-458 (2011).
52. S. A. Rogers, Journal of rheology **56** (5), 1129-1151 (2012).
53. G. J. Donley, P. K. Singh, A. Shetty and S. A. Rogers, Proceedings of the National Academy of Sciences **117** (36), 21945-21952 (2020).
54. P. Ptaszek, Journal of Food Engineering **146**, 53-61 (2015).
55. M. Y. Erturk, S. A. Rogers and J. Kokini, Food Hydrocolloids **128**, 107558 (2022).
56. J. D. Park and S. A. Rogers, Physics of Fluids **32** (6), 063102 (2020).
57. M. Mermet-Guyennet, J. Gianfelice de Castro, M. Habibi, N. Martzel, M. Denn and D. Bonn, Journal of Rheology **59** (1), 21-32 (2015).
58. J. Sandler, M. Shaffer, T. Prasse, W. Bauhofer, K. Schulte and A. Windle, Polymer **40** (21), 5967-5971 (1999).
59. S. Witpathomwong, M. Okhawilai, C. Jubsilp, P. Karagiannidis and S. Rimdusit, International Journal of Hydrogen Energy **45** (55), 30898-30910 (2020).
60. K.-H. Ahn, H. Kyu, J.-G. Nam, W. Manfred and S.-J. Lee, Korea-Australia Rheology Journal **15** (2), 97-105 (2003).
61. K. Hyun, S. H. Kim, K. H. Ahn and S. J. Lee, Journal of Non-Newtonian Fluid Mechanics **107** (1-3), 51-65 (2002).
62. E. Feilden, 2017.
63. S. Tagliaferri, A. Panagiotopoulos and C. Mattevi, Materials Advances **2** (2), 540-563 (2021).
64. J. E. Smay, J. Cesarano and J. A. Lewis, Langmuir **18** (14), 5429-5437 (2002).
65. J. Orangi, F. Hamade, V. A. Davis and M. Beidaghi, ACS nano **14** (1), 640-650 (2019).
66. W. Li, Y. Li, M. Su, B. An, J. Liu, D. Su, L. Li, F. Li and Y. Song, Journal of Materials Chemistry A **5** (31), 16281-16288 (2017).
67. Z. Qi, J. Ye, W. Chen, J. Biener, E. B. Duoss, C. M. Spadaccini, M. A. Worsley and C. Zhu, Advanced Materials Technologies **3** (7), 1800053 (2018).
68. X. Tang, H. Zhou, Z. Cai, D. Cheng, P. He, P. Xie, D. Zhang and T. Fan, ACS nano **12** (4), 3502-3511 (2018).
69. Z. Wang, Q. e. Zhang, S. Long, Y. Luo, P. Yu, Z. Tan, J. Bai, B. Qu, Y. Yang and J. Shi, ACS applied materials & interfaces **10** (12), 10437-10444 (2018).
70. T. Wang, X. Tian, L. Li, L. Lu, S. Hou, G. Cao and H. Jin, Journal of Materials Chemistry A **8** (4), 1749-1756 (2020).

FIGURE 1

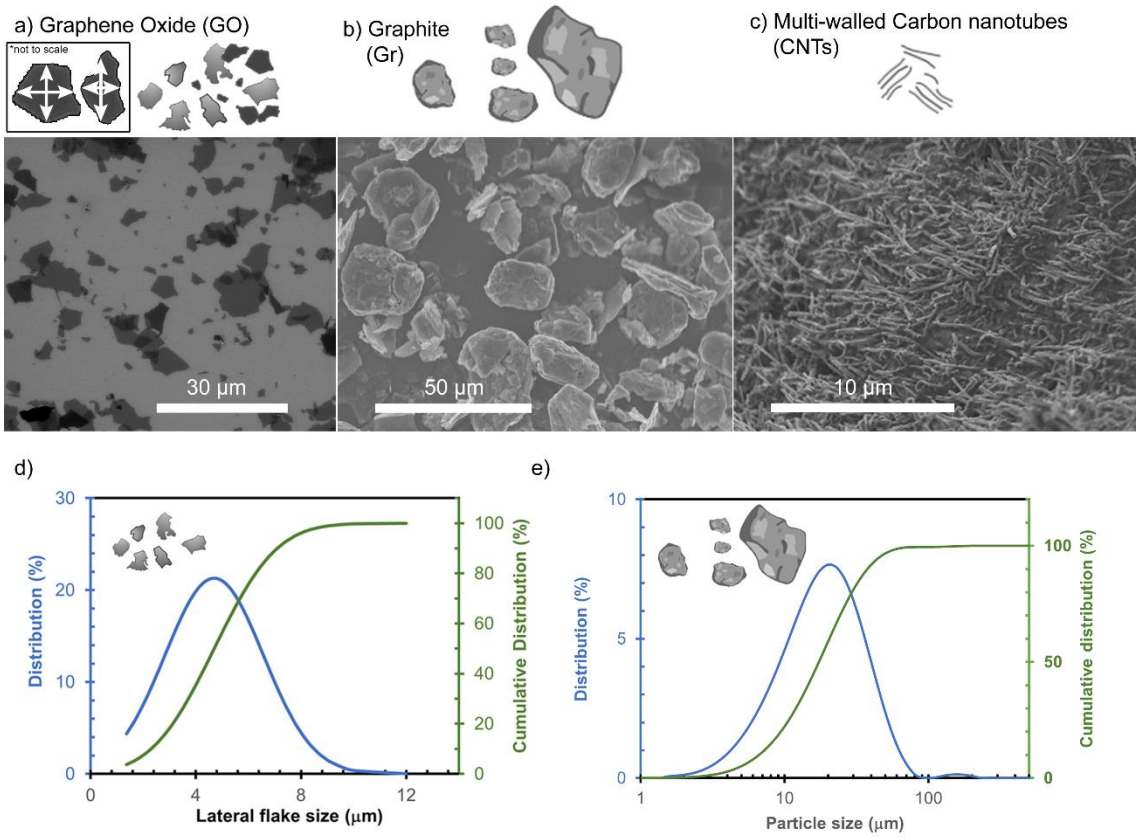
a) Graphene Oxide (GO)
*not to scale
b) Graphite (Gr)
c) Multi-walled Carbon nanotubes (CNTs)
30 µm
50 µm
10 µm
d)
Distribution (%)
Cumulative Distribution (%)
Lateral flake size (µm)
e)
Distribution (%)
Cumulative distribution (%)
Particle size (µm)

FIGURE 2

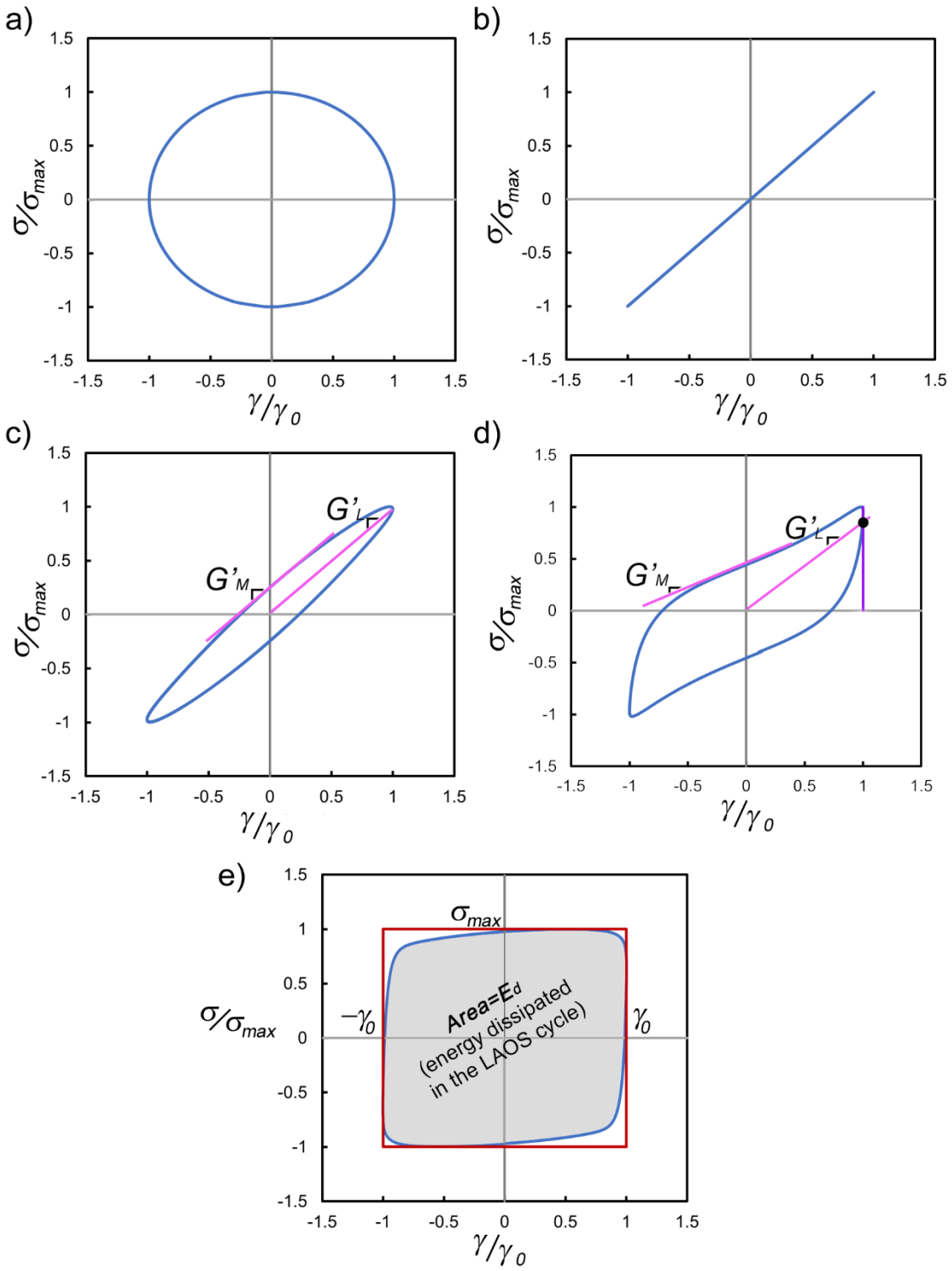
a)
b)
c)
d)
e)
σ/σmax
γ/γ0
G'L
G'M
σmax
−γ0
γ0
Area=Ed
(energy dissipated
in the LAOS cycle)

FIGURE 3

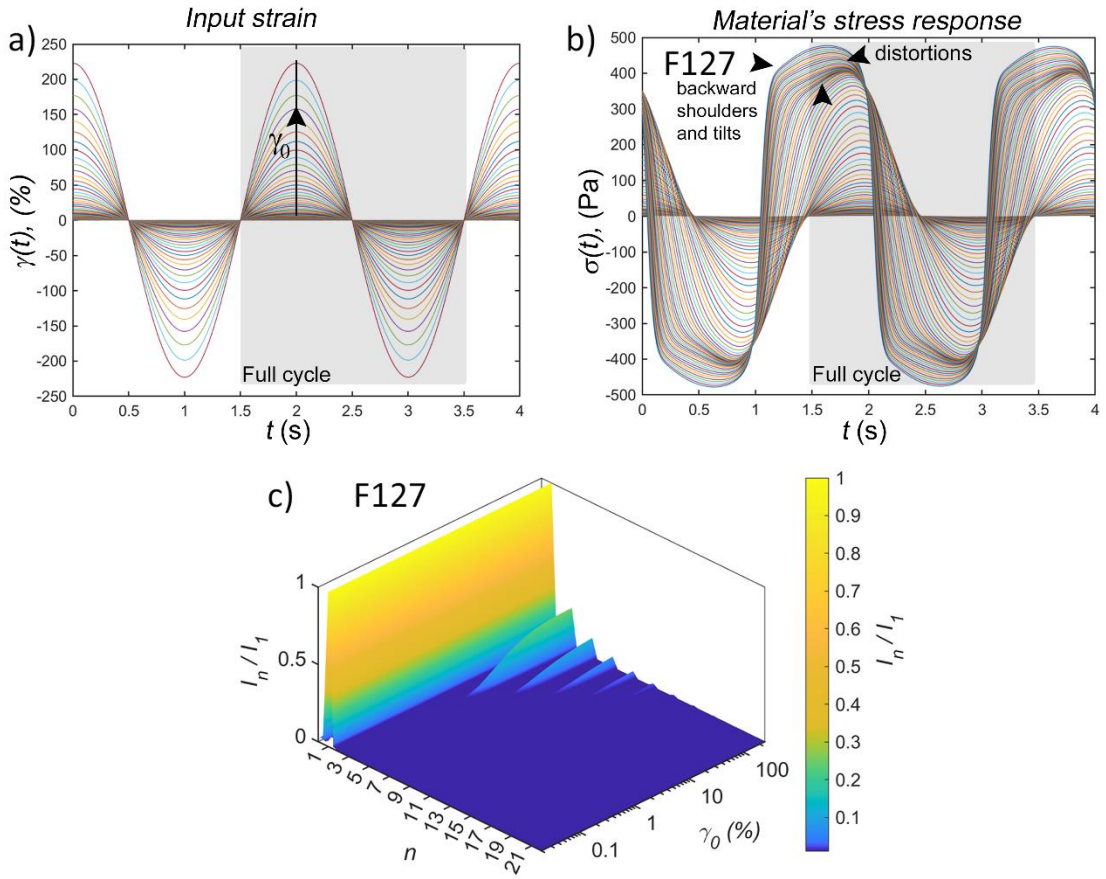
a)
Input strain
γ(t), (%)
t (s)
γ0
Full cycle
b)
Material's stress response
σ(t), (Pa)
t (s)
F127
backward
shoulders
and tilts
distortions
Full cycle
c)
F127
In / I1
n
γ0 (%)

FIGURE 4

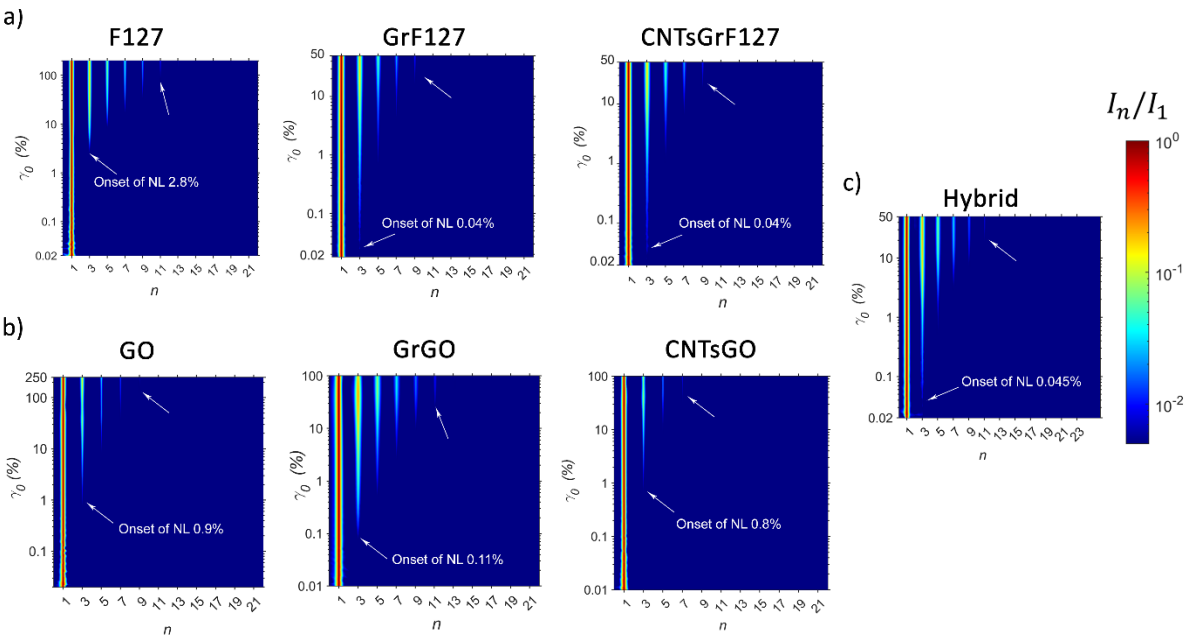
a)
F127
GrF127
CNTsGrF127
Onset of NL 2.8%
Onset of NL 0.04%
Onset of NL 0.04%
b)
GO
GrGO
CNTsGO
Onset of NL 0.9%
Onset of NL 0.11%
Onset of NL 0.8%
c)
Hybrid
Onset of NL 0.045%
I_n/I_1
γ_0 (%)
n

FIGURE 5

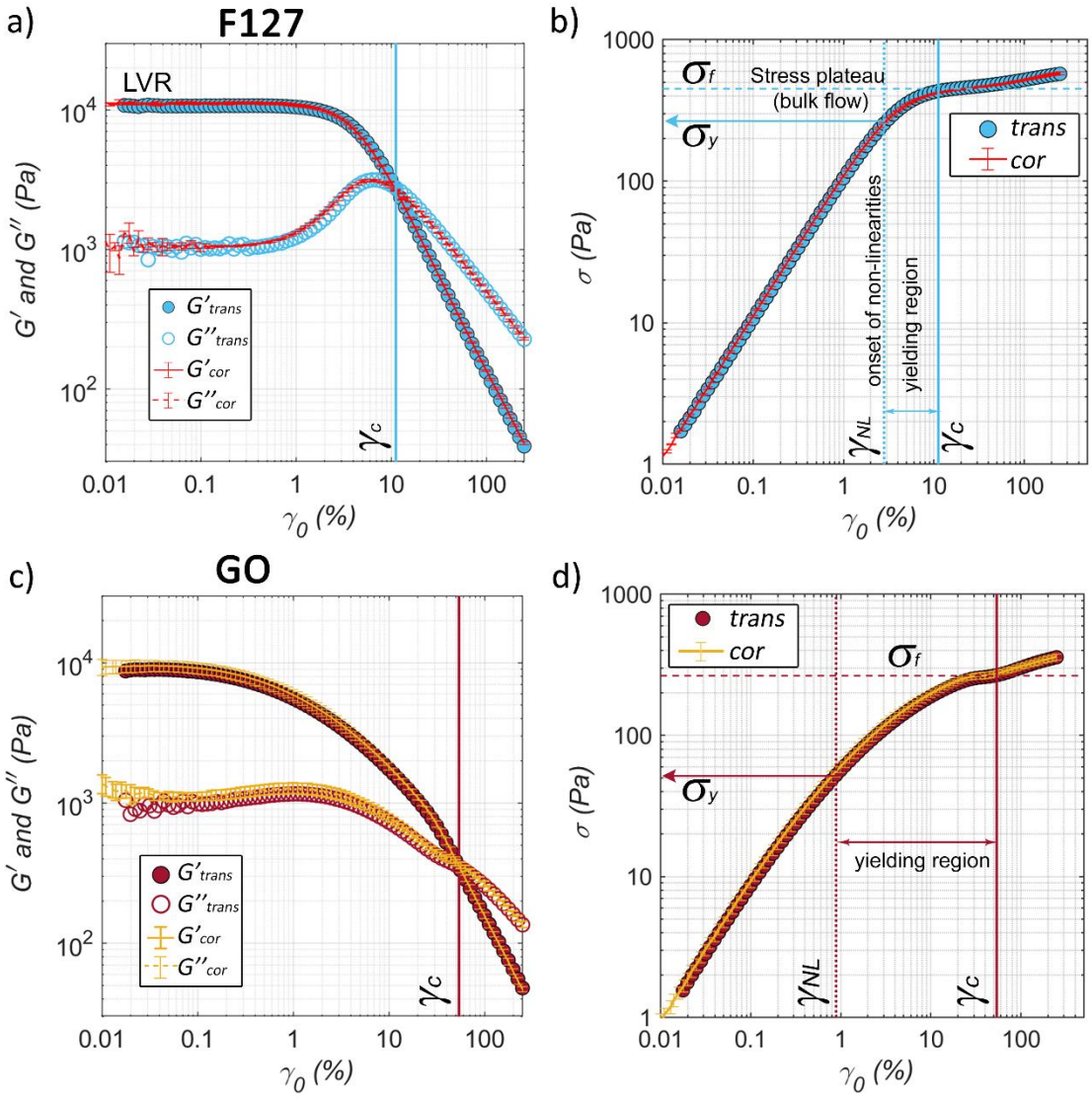
a)
F127
LVR
G′ and G″ (Pa)
10^4
10^3
10^2
G'_{trans}
G''_{trans}
G'_{cor}
G''_{cor}
γ_c
0.01
0.1
1
10
100
γ_0 (%)
b)
1000
100
10
1
σ (Pa)
σ_f
Stress plateau
(bulk flow)
σ_y
trans
cor
onset of non-linearities
yielding region
γ_{NL}
γ_c
γ_0 (%)
c)
GO
G′ and G″ (Pa)
10^4
10^3
10^2
G'_{trans}
G''_{trans}
G'_{cor}
G''_{cor}
γ_c
0.01
0.1
1
10
100
γ_0 (%)
d)
1000
100
10
1
σ (Pa)
trans
cor
σ_f
σ_y
yielding region
γ_{NL}
γ_c
γ_0 (%)

FIGURE 6

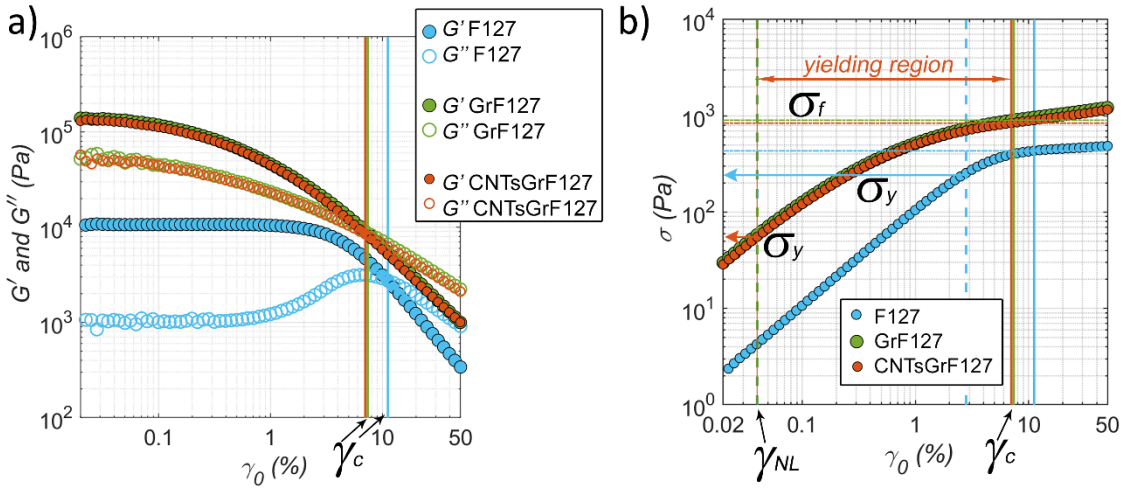
a)
G' F127
G'' F127
G' GrF127
G'' GrF127
G' CNTsGrF127
G'' CNTsGrF127
G' and G'' (Pa)
γ0 (%)
γc
b)
yielding region
σf
σy
σy
σ (Pa)
F127
GrF127
CNTsGrF127
γNL
γ0 (%)
γc

FIGURE 7

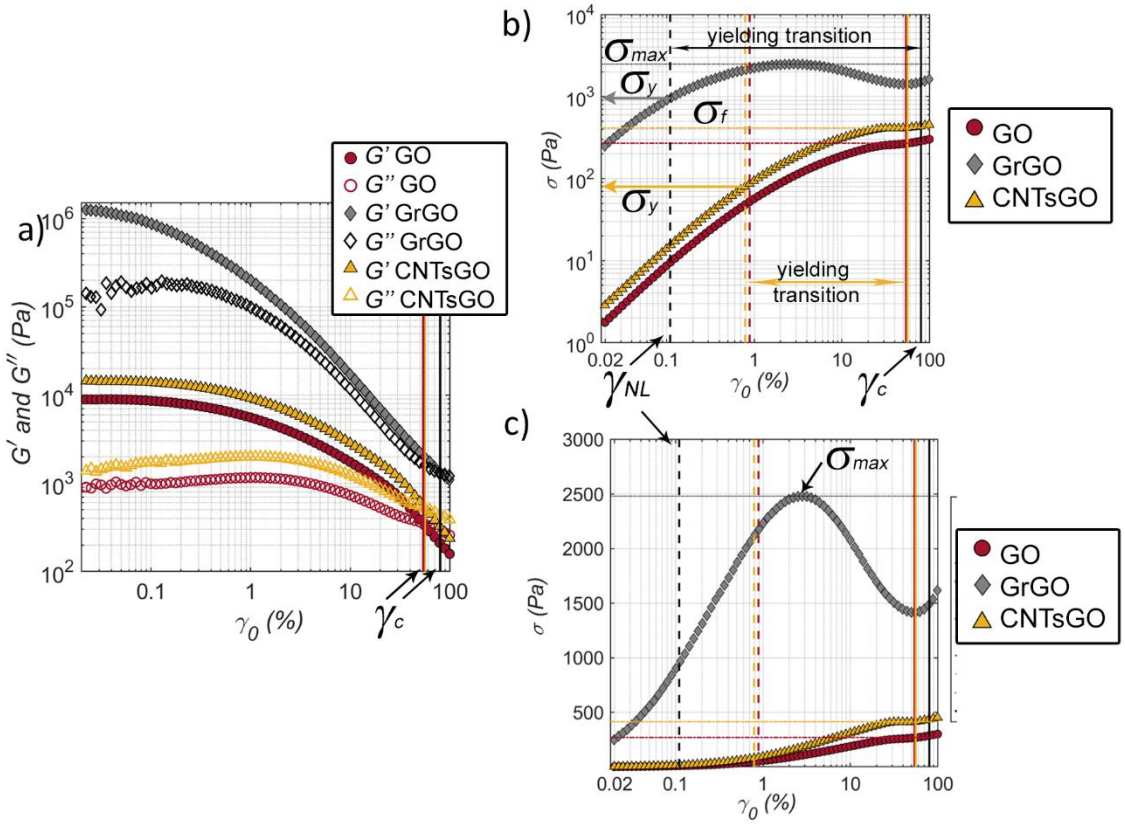
a)
G' GO
G'' GO
G' GrGO
G'' GrGO
G' CNTsGO
G'' CNTsGO
G' and G'' (Pa)
γ0 (%)
γc
b)
σmax
yielding transition
σy
σf
σy
yielding transition
σ (Pa)
γNL
γ0 (%)
γc
GO
GrGO
CNTsGO
c)
σmax
σ (Pa)
γ0 (%)
GO
GrGO
CNTsGO

FIGURE 8

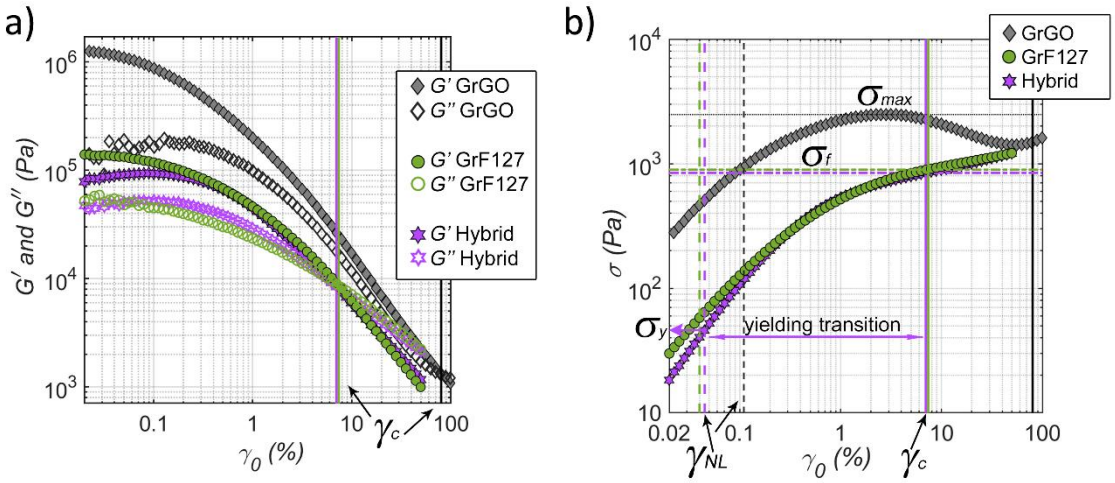
a)
b)
G′ GrGO
G″ GrGO
G′ GrF127
G″ GrF127
G′ Hybrid
G″ Hybrid
G′ and G″ (Pa)
γ0 (%)
γc
GrGO
GrF127
Hybrid
σmax
σf
σy
yielding transition
σ (Pa)
γNL
γc

FIGURE 9

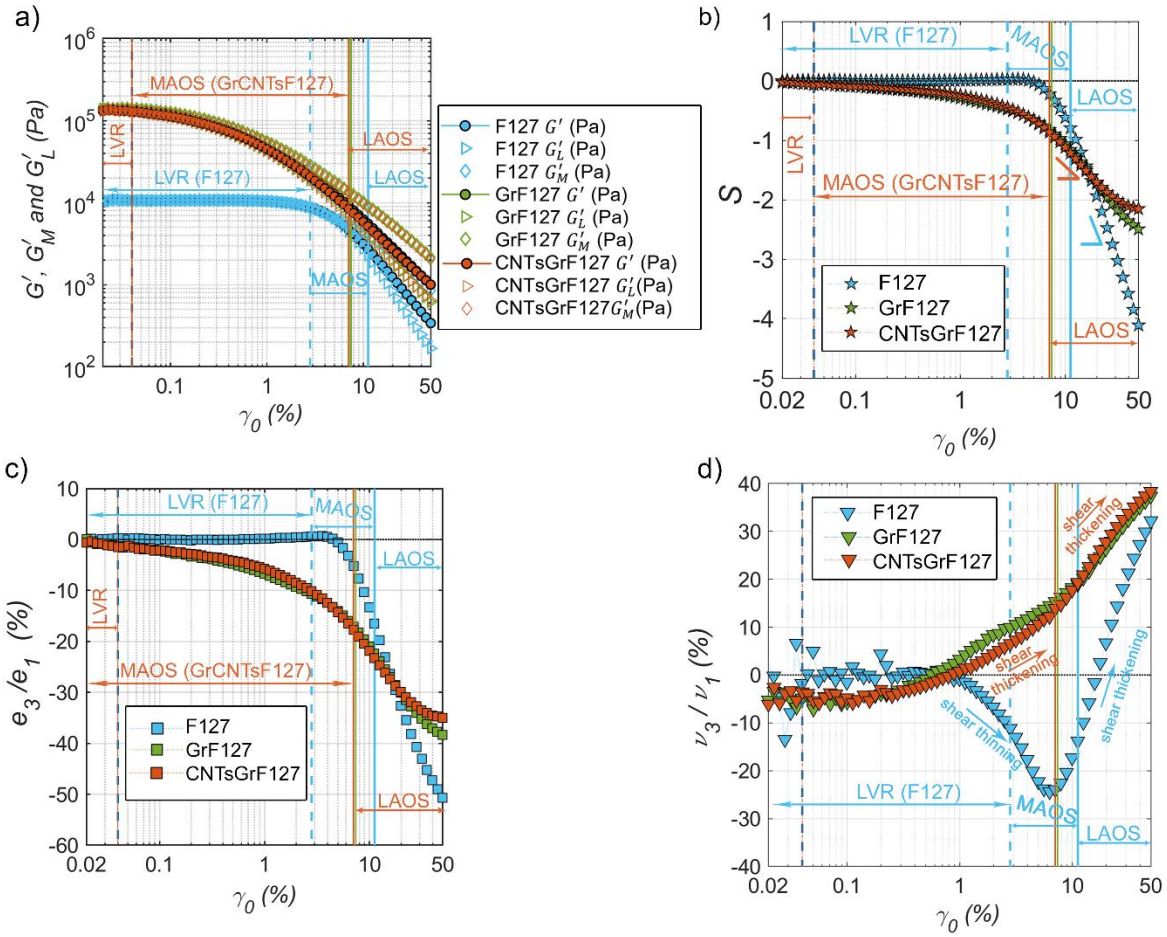
a)
b)
c)
d)
LVR
MAOS (GrCNTsF127)
LVR (F127)
LAOS
MAOS
γ_0 (%)
G', G'_M and G'_L (Pa)
F127 G' (Pa)
F127 G'_L (Pa)
F127 G'_M (Pa)
GrF127 G' (Pa)
GrF127 G'_L (Pa)
GrF127 G'_M (Pa)
CNTsGrF127 G' (Pa)
CNTsGrF127 G'_L(Pa)
CNTsGrF127G'_M(Pa)
S
F127
GrF127
CNTsGrF127
e_3/e_1 (%)
ν_3/ν_1 (%)
shear thickening
shear thinning

FIGURE 10

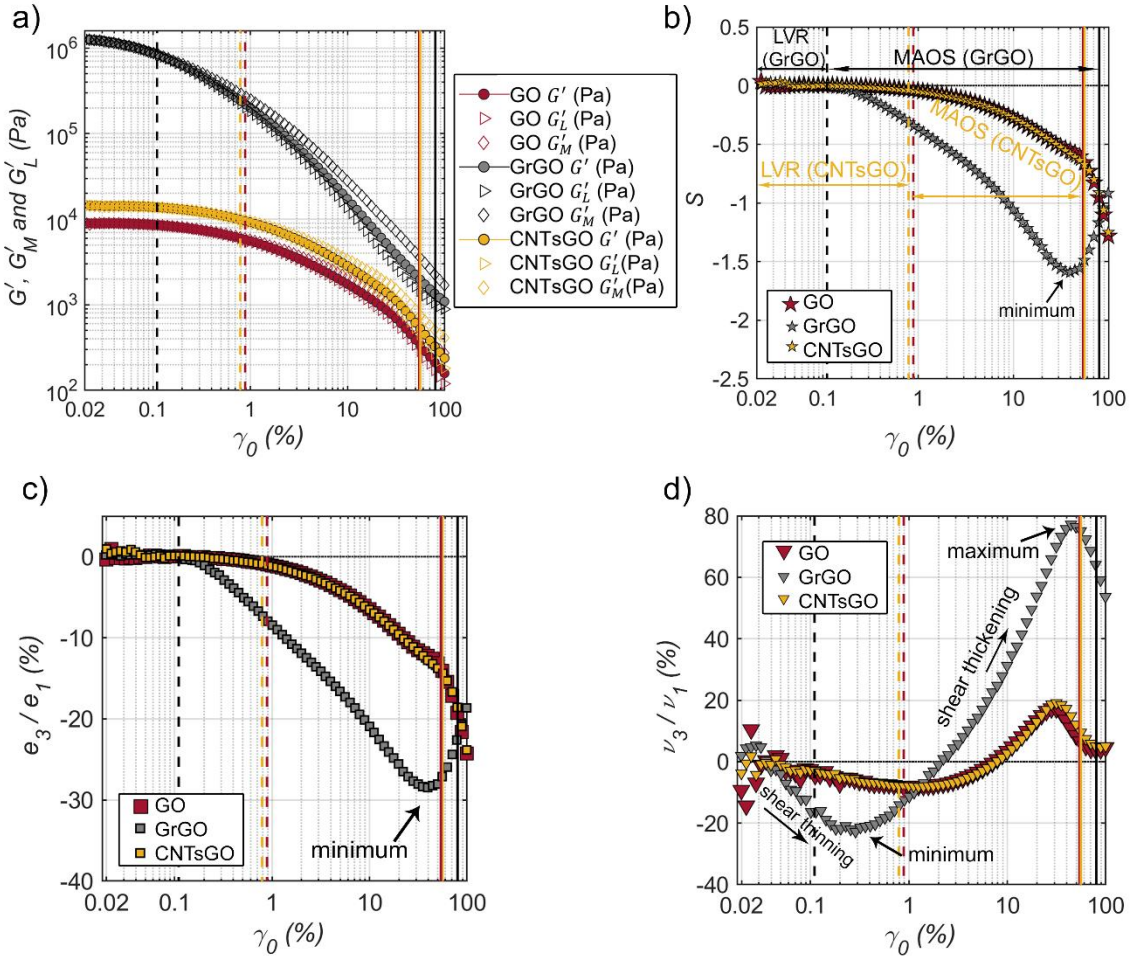
a)
b)
c)
d)
GO G' (Pa)
GO G'_L (Pa)
GO G'_M (Pa)
GrGO G' (Pa)
GrGO G'_L (Pa)
GrGO G'_M (Pa)
CNTsGO G' (Pa)
CNTsGO G'_L(Pa)
CNTsGO G'_M(Pa)
G', G'_M and G'_L (Pa)
γ_0 (%)
LVR (GrGO)
MAOS (GrGO)
LVR (CNTsGO)
MAOS (CNTsGO)
S
minimum
GO
GrGO
CNTsGO
e_3 / e_1 (%)
v_3 / v_1 (%)
maximum
shear thickening
shear thinning

FIGURE 11

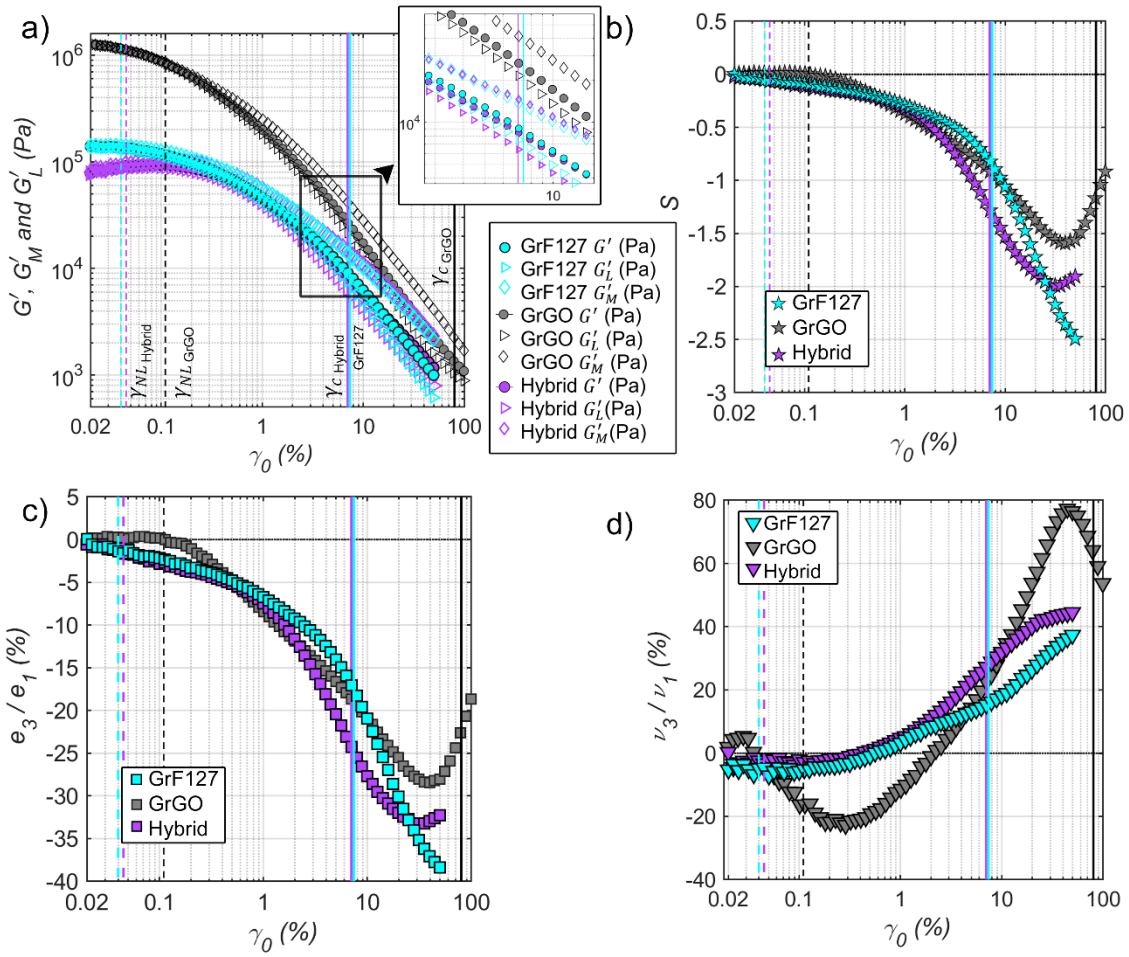
a)
b)
c)
d)
G', G'_M and G'_L (Pa)
γ_0 (%)
$\gamma_{NL\ Hybrid}$
$\gamma_{NL\ GrGO}$
$\gamma_{c\ Hybrid}$
GrF127
$\gamma_{c\ GrGO}$
GrF127 G' (Pa)
GrF127 G'_L (Pa)
GrF127 G'_M (Pa)
GrGO G' (Pa)
GrGO G'_L (Pa)
GrGO G'_M (Pa)
Hybrid G' (Pa)
Hybrid G'_L(Pa)
Hybrid G'_M(Pa)
S
GrF127
GrGO
Hybrid
e_3 / e_1 (%)
ν_3 / ν_1 (%)

FIGURE 12

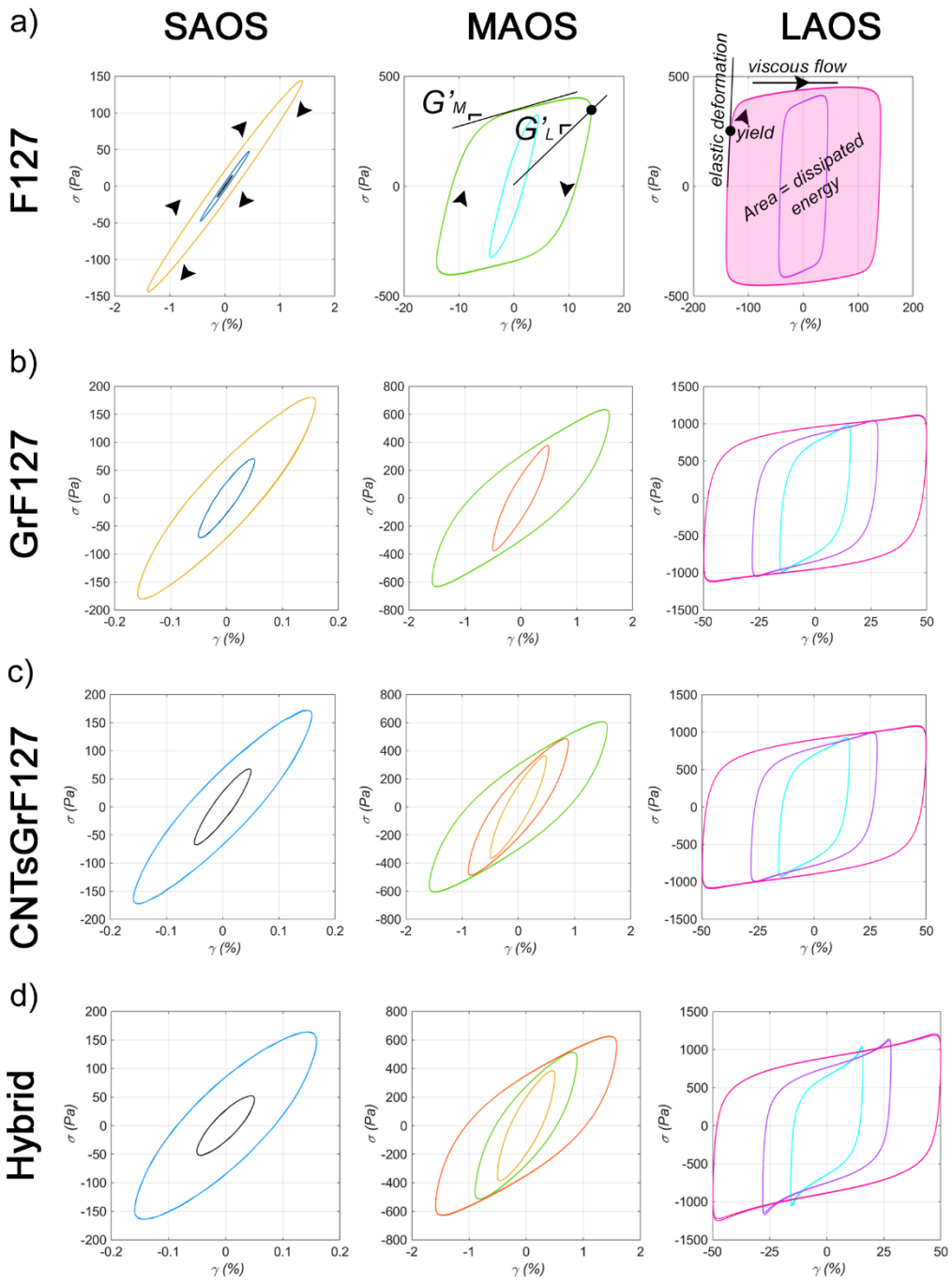
a)
SAOS
MAOS
LAOS
F127
b)
GrF127
c)
CNTsGrF127
d)
Hybrid
σ (Pa)
γ (%)
G'M
G'L
viscous flow
elastic deformation
yield
Area = dissipated energy

FIGURE 13

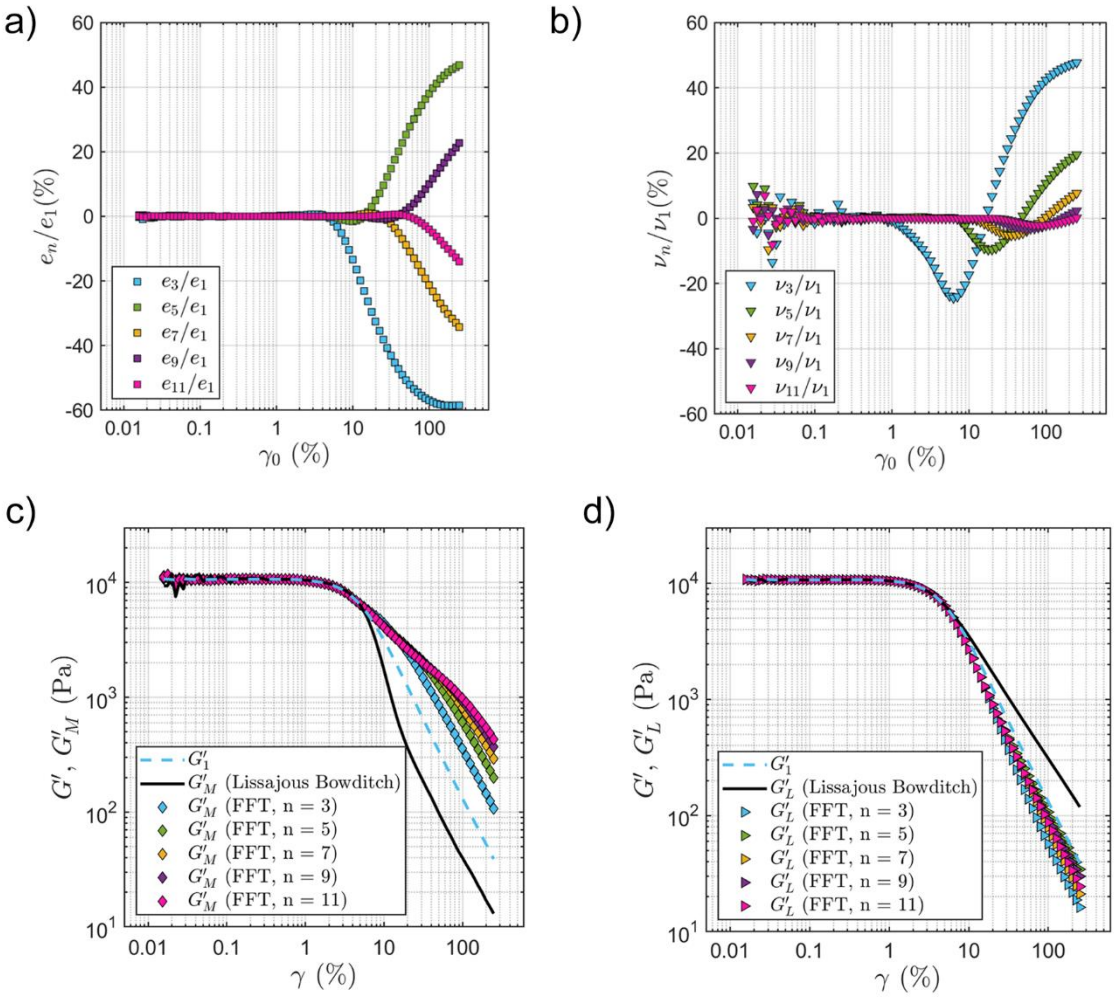
a)
b)
c)
d)
e_n/e_1 (%)
ν_n/ν_1 (%)
γ_0 (%)
e_3/e_1
e_5/e_1
e_7/e_1
e_9/e_1
e_{11}/e_1
ν_3/ν_1
ν_5/ν_1
ν_7/ν_1
ν_9/ν_1
ν_{11}/ν_1
G', G'_M (Pa)
G', G'_L (Pa)
γ (%)
G'_1
G'_M (Lissajous Bowditch)
G'_M (FFT, n = 3)
G'_M (FFT, n = 5)
G'_M (FFT, n = 7)
G'_M (FFT, n = 9)
G'_M (FFT, n = 11)
G'_L (Lissajous Bowditch)
G'_L (FFT, n = 3)
G'_L (FFT, n = 5)
G'_L (FFT, n = 7)
G'_L (FFT, n = 9)
G'_L (FFT, n = 11)

FIGURE 14

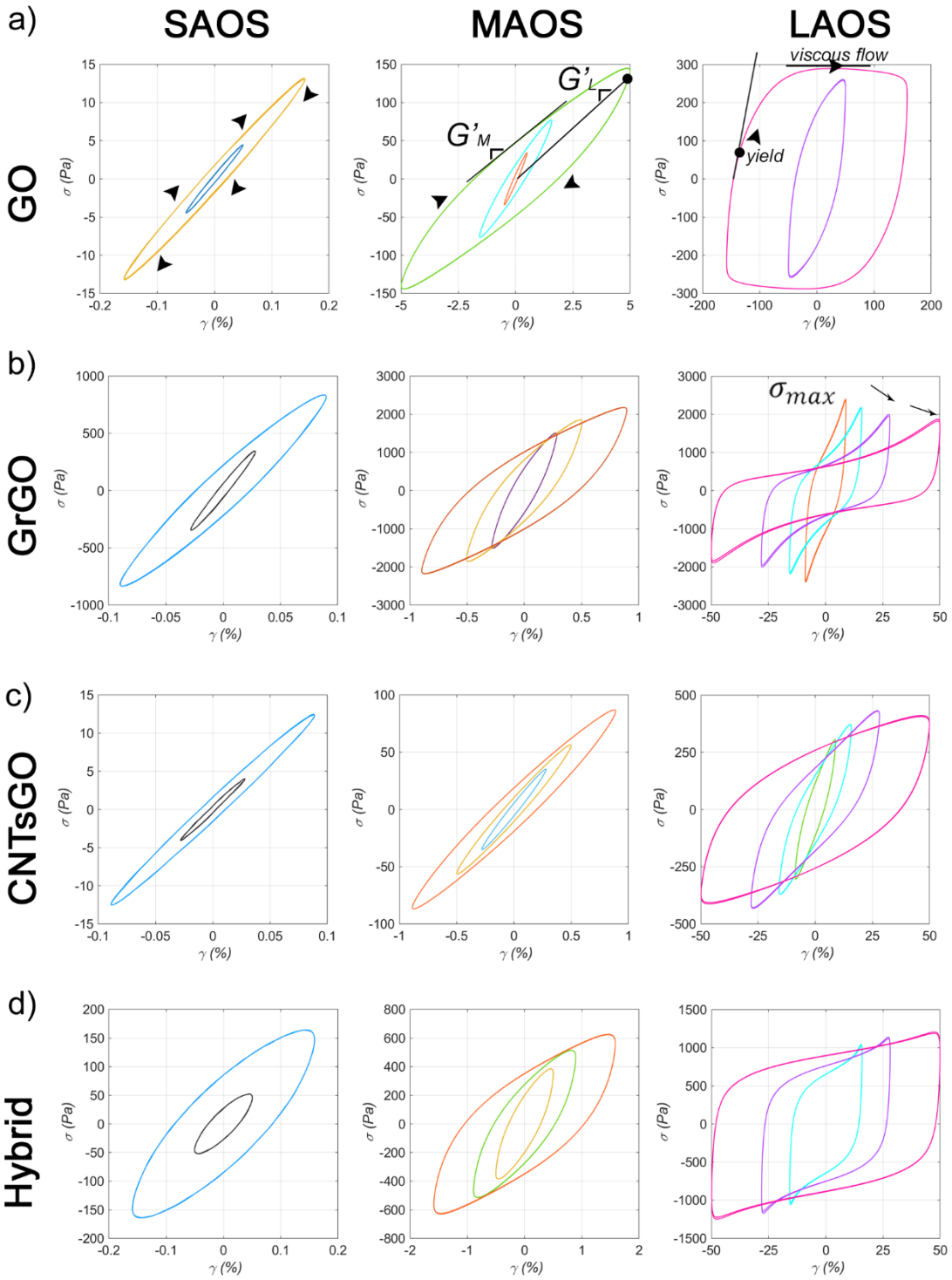
a)
SAOS
MAOS
LAOS
GO
viscous flow
yield
G'L
G'M
b)
GrGO
σmax
c)
CNTsGO
d)
Hybrid
σ (Pa)
γ (%)

FIGURE 15

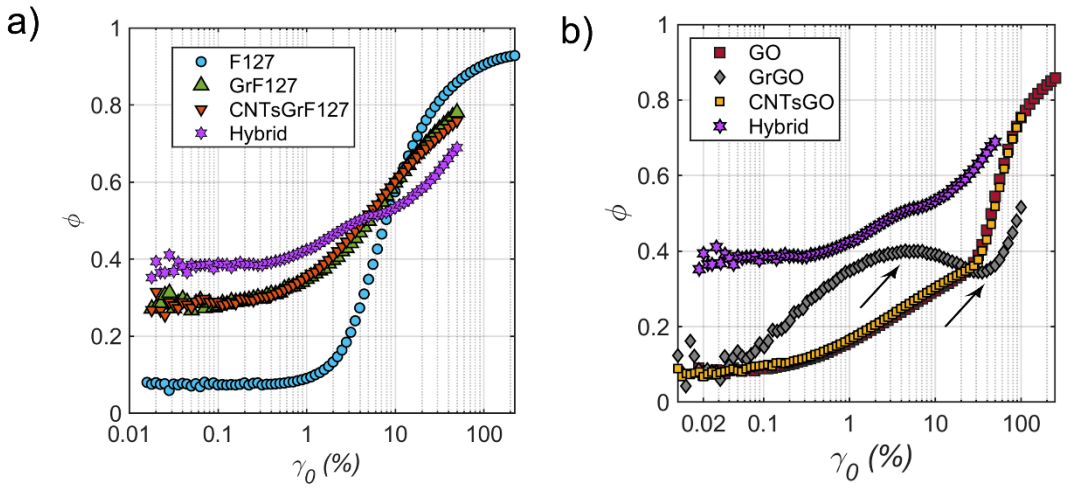
a)
F127
GrF127
CNTsGrF127
Hybrid
ϕ
γ_0 (%)
b)
GO
GrGO
CNTsGO
Hybrid
ϕ
γ_0 (%)

FIGURE 16

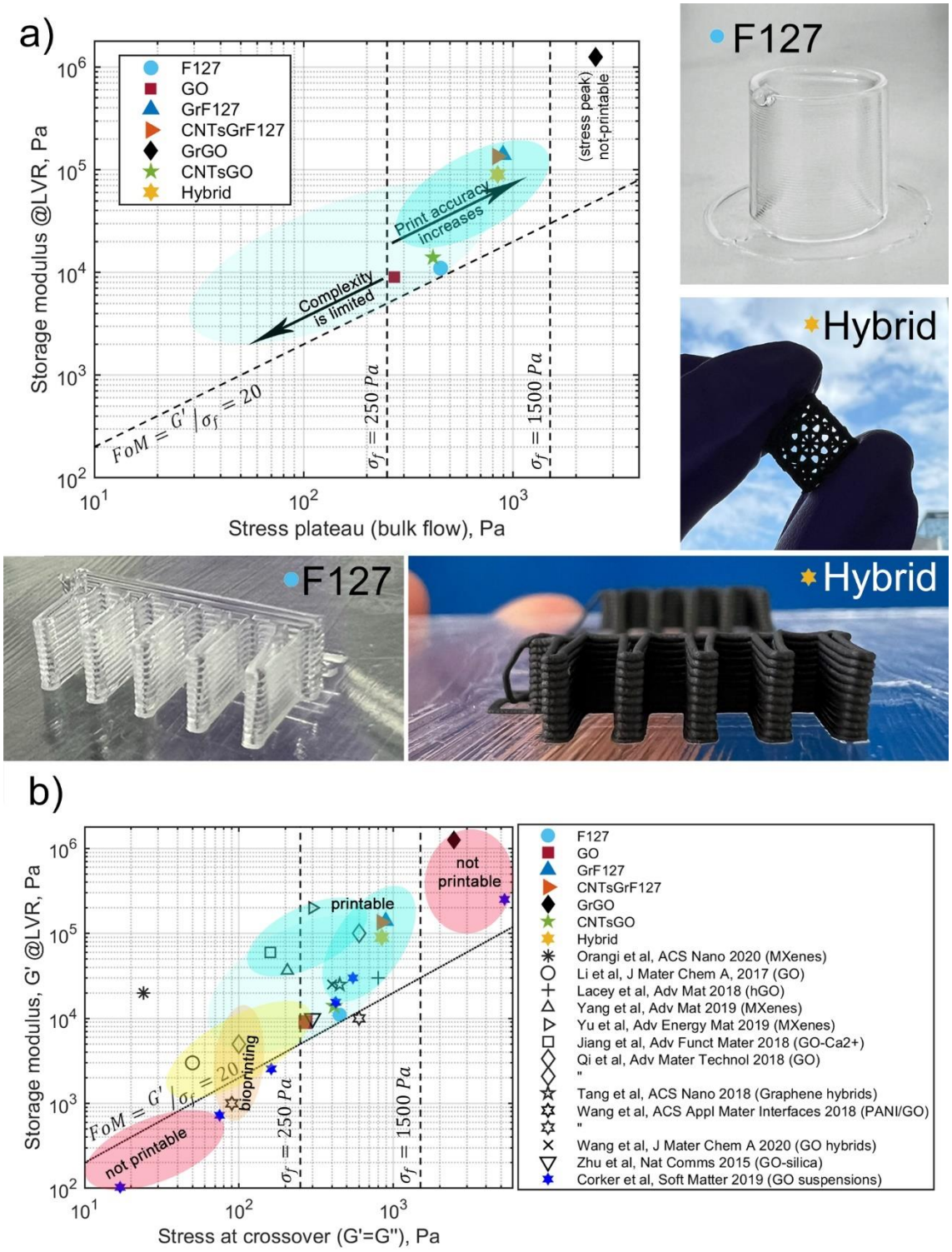
a)
F127
GO
GrF127
CNTsGrF127
GrGO
CNTsGO
Hybrid
Storage modulus @LVR, Pa
Stress plateau (bulk flow), Pa
Print accuracy increases
Complexity is limited
(stress peak) not-printable
$FoM = G' \mid \sigma_f = 20$
$\sigma_f = 250\ Pa$
$\sigma_f = 1500\ Pa$
F127
Hybrid
F127
Hybrid
b)
Storage modulus, G' @LVR, Pa
Stress at crossover (G'=G''), Pa
not printable
printable
bioprinting
not printable
$FoM = G' \mid \sigma_f = 20$
$\sigma_f = 250\ Pa$
$\sigma_f = 1500\ Pa$
F127
GO
GrF127
CNTsGrF127
GrGO
CNTsGO
Hybrid
Orangi et al, ACS Nano 2020 (MXenes)
Li et al, J Mater Chem A, 2017 (GO)
Lacey et al, Adv Mat 2018 (hGO)
Yang et al, Adv Mat 2019 (MXenes)
Yu et al, Adv Energy Mat 2019 (MXenes)
Jiang et al, Adv Funct Mater 2018 (GO-Ca2+)
Qi et al, Adv Mater Technol 2018 (GO)
"
Tang et al, ACS Nano 2018 (Graphene hybrids)
Wang et al, ACS Appl Mater Interfaces 2018 (PANI/GO)
"
Wang et al, J Mater Chem A 2020 (GO hybrids)
Zhu et al, Nat Comms 2015 (GO-silica)
Corker et al, Soft Matter 2019 (GO suspensions)